Photoelectron Circular Dichroism of Bicyclic Ketones from Multiphoton Ionization with Femtosecond Laser Pulses

Christian Lux,[a] Matthias Wollenhaupt,[b] Cristian Sarpe,[a] and Thomas Baumert*[a]

Photoelectron circular dichroism (PECD) is a CD effect up to the ten-percent regime and shows contributions from higher-order Legendre polynomials when multiphoton ionization is compared to single-photon ionization. We give a full account of our experimental methodology for measuring the multiphoton PECD and derive quantitative measures that we apply on camphor, fenchone and norcamphor. Different modulations and amplitudes of the contributing Legendre polynomials are observed despite the similarity in chemical structure. In addi-tion, we study PECD for elliptically polarized light employing tomographic reconstruction methods. Intensity studies reveal dissociative ionization as the origin of the observed PECD effect, whereas ionization of the intermediate resonance is dominating the signal. As a perspective, we suggest to make use of our tomographic data as an experimental basis for a complete photoionization experiment and give a prospect of PECD as an analytic tool.

1. Introduction

Chirality plays an important role in nearly all areas of fundamental and applied science, as the interaction of chiral objects with each other often depends on their handedness. Prominent examples are the interaction of chiral drugs with the corresponding chiral receptors in the human body, giving rise to different follow-up reactions, or the interaction of circularly polarized light with chiral molecules, giving rise to different chiroptical effects. The first example highlights the importance of developing ultrasensitive and fast methods for chiral analysis and the second hints to a convenient way to perform such an analysis, that is, to distinguish different enantiomers, determine enantiomeric excess or even assigning the absolute stereochemical configuration.

Working in the gas phase under collision-free conditions is beneficial for both aspects. Because low particle densities are involved, highly sensitive methods might be developed and because usually collision- and interaction-free conditions are achieved, a more fundamental understanding of the light–matter interaction can be expected, leading finally to additional approaches for the abovementioned assignment of the absolute configuration.

In this spirit, new gas-phase methods have been developed very recently and are reviewed in a perspective article.[1] The techniques can be divided into two classes. One relies on pho-toionization, the other on microwave three-wave mixing in seeded molecular beams,[2] where the latter is the main focus of the abovementioned perspective article.

Photoionization approaches benefit from nearly unit detection efficiencies of charged particles and differ in the detection scheme ranging from the measurement of mass spectra to imaging of photoelectron angular distributions to sophisticated photoion–photoelectron coincidence techniques. These detection schemes also reflect different aspects of the light–matter interaction. Mass spectroscopy together with resonance-enhanced multiphoton ionization (REMPI) exploits usually differences in the magnetic and electric dipole moments of the resonant intermediate. Nanosecond as well as femtosecond laser sources have been used in corresponding circular dichroism (CD) experiments[3–5] and are reviewed in Ref. [6]. Coincidence techniques have recently been used to directly determine the absolute molecular stereochemistry after laser-induced[7] and foil-induced Coulomb explosions.[8]

A distinctive asymmetry in the differential photoionization cross section from the ionization of randomly oriented chiral molecules with circularly polarized light was theoretically predicted by Ritchie in 1976[9] based on the electric dipole approximation. This asymmetry is reflected in the electron ejection, or rather the photoelectron angular distribution (PAD). A change in direction with respect to the light propagation direction is observed dependent on the handedness of the enantiomer and the handedness of the ionizing light. This CD effect was termed photoelectron circular dichroism (PECD).[10]

Since PECD is an electric dipole effect, it can be several orders of magnitude larger than conventionally measured CD and is therefore promising with regard to spectroscopic studies of chiral species in the gas phase. During the last decade, PECD was investigated on many small chiral molecules using one-photon vacuum ultraviolet (VUV) synchrotron radiation

[a] C. Lux, C. Sarpe, Prof. Dr. T. Baumert
Institut für Physik und CINSaT
Universität Kassel
Heinrich-Plett-Straße 40, 34132 Kassel (Germany)
E-mail: tbaumert@uni-kassel.de

[b] Prof. Dr. M. Wollenhaupt
Institut für Physik
Carl von Ossietzky Universität Oldenburg
Carl-von-Ossietzky-Straße 9-11, 26129 Oldenburg (Germany)

and angle-resolved emission detection,[11–15] later applying velocity-map imaging (VMI) techniques.[10,16] The developments of PECD via one-photon ionization are reviewed in Chapter 1 of Ref. [17] by Nahon and Powis and in Ref. [18]. In addition, chiral dimers[19] and clusters[20] have been studied for PECD effects. The influence of excited ion vibrational modes on the PECD was lately determined.[21]

Recently, we have demonstrated that PADs from randomly oriented chiral molecules in a femtosecond REMPI process reveal a highly structured PECD in the $\pm 10\%$ regime that can be measured with the help of VMI techniques using a table-top set-up.[22] From an application point of view, a widespread implementation of this effect is now opened to analytics, because the necessity of synchrotron facilities to deliver the required radiation seems not to be a prerequisite anymore and producing circularly polarized VUV radiation from laser-based high-harmonic sources is still a technological challenge.[23,24] From a scientific point of view the REMPI nature of the process can be used to explore the nuclear and electron dynamics of the intermediate resonance in the future with the help of coherent control techniques.[25] Within that context femtosecond time-resolved photoelectron spectroscopy[26,27] has been used to study nuclear dynamics[26,28] as well as changes in the electronic structure[29] on electronically excited molecular states. Direct control of charge oscillations for molecular excitation[30] as well as the generation and detection of atomic ring currents[31] has been demonstrated. In addition, it has been shown that polarization-shaped laser pulses give access to the vectorial aspects of light–matter interaction[32] and that the momentum distribution of photoelectrons resulting from multiphoton ionization with polarization-shaped laser pulses can be crafted in a sophisticated fashion[33] and detected with the help of tomographic reconstruction methods.[34] On atoms, the combination of these techniques was recently used to perform a complete photoionization experiment.[35]

As prototypes, the enantiomers of camphor and fenchone have been chosen in our original study because their normal CD as well as their PECD has been studied extensively using VUV one-photon ionization.[10–13,16,19] The results on camphor have been reproduced very recently with the help of coincidence measurements[36,37] and are reviewed also with respect to one-photon ionization in Ref. [38].

In this contribution we give a comprehensive account of our PECD studies. We reproduce our results on camphor and fenchone[22] and extend them to norcamphor. In addition we derive quantification measures for the PECD effect and present an ellipticity study as well as an intensity study. The paper is structured as follows:

We start by giving a brief overview of PADs resulting from multiphoton ionization of isotropically distributed molecules and derive different measures to quantify the PECD effect. A detailed description and characterization of our experimental set-up and the data evaluation is given next. In the same section the measurement procedure and data evaluation is verified on (achiral) Xenon. With the help of the camphor prototype we discuss in detail the data acquisition, data evaluation and application of different quantification measures. We con-

tinue with an ellipticity study of the PECD effect, where we break the cylindrical symmetry of the photoelectron angular distribution. We apply and discuss a tomographic reconstruction method to that end and compare for circularly polarized light tomographic reconstruction to Abel inversion. With the help of intensity studies we identify dissociative ionization as the origin of the observed PECD effect and also present evidence that the observed photoelectron signal stems from ionization of an intermediate resonance and not from ground-state ionization. Next, a comparison to other recently published results is given. We then discuss the PECD results from chemically similar bicyclic ketones. There are pronounced differences in the PECD despite the similarity of their chemical structure. We end with a short demonstration of PECD as an analytical tool to determine enantiomeric excess.

2. Quantification of Multiphoton PECD

In order to quantitatively describe the experimental results we start by considering the general symmetry properties of the photoelectron angular distributions and the corresponding PAD images. The relevant physical quantity, that is, the three-dimensional photoelectron density $\rho(x,y,z)$ is analysed and quantitative measures are derived from the electron density. In addition, their relation to the measured PAD images is described.

Photoelectron angular distributions for a given excess energy resulting from multiphoton ionization of isotropically distributed molecules can be expanded into spherical harmonics, which reduce to an expansion of Legendre polynomials P_l for linearly (LIN) or circularly polarized light and corresponding Legendre coefficients c_l [Eq. (1)]:[39–43]

$$P(\Theta) \propto \sum_{l=0}^{l_{max}} c_l P_l[\cos(\Theta)] \tag{1}$$

These distributions $P(\Theta)$ are cylindrically symmetric. In the LIN case the symmetry axis is the polarization vector and in the cases of left (LCP) or right circularly polarized (RCP) light it is the light propagation, that is, the k vector. Θ is the angle measured between the symmetry axis and the ejection direction of the photoelectron (see Figure 1 for circularly polarized light). Even Legendre polynomials are symmetric with respect to the light propagation, taking the y-axis as mirror axis, whereas odd Legendre polynomials are antisymmetric. With reference to Yang's theorem,[44] which was first applied to nuclear scattering processes, the maximum order of Legendre polynomials in this sum is usually given as $l_{max} = 2n$ where n is the number of photons required for ionization (see Ref. [45]). In single-photon ionization of atoms[46] or in case of isotropically distributed achiral molecules[47,48] this expansion has to be executed up to the second Legendre polynomial with no contribution by P_1.

In the case of randomly oriented chiral molecules and circularly polarized single-photon ionization, the first Legendre polynomial, that is, an odd-order Legendre polynomial has to be considered additionally. The amplitude of this first-order

Legendre polynomial has been numerically calculated[49, 50] and experimentally determined with the help of PECD measurements using synchrotron radiation.[10–16,18–21,51] As a matter of parity conservation[52] this odd-order polynomial changes its sign either on exchanging the enantiomer or the helicity of light.

PADs containing high-order odd Legendre polynomials—that alter sign by changing the enantiomer or helicity of light—were recently observed.[22] They result from multiphoton ionization of randomly oriented chiral molecules, using circularly polarized femtosecond laser pulses.

We now turn to the topic of deriving quantitative measures for multiphoton PECD. In an ideal experiment, a single measurement on a specific enantiomer with one of the two helicities would be sufficient for PECD determinations as changing the helicity of light or the enantiomer only leads to a change in sign of the odd polynomials. The even polynomials stay unchanged. For example, with the help of VMI techniques, the projection of a PAD from one enantiomer with circularly polarized light of specific helicity could be measured. After an Abel inversion[53] information on the contributing even and odd Legendre coefficients could be derived. In a real experiment, however, additional symmetric and antisymmetric parts in the measured PAD images may arise due to experimental imperfections. Examples for such imperfections are detector inhomogeneities, off-center projections or inaccuracies in the circular polarization states.

A first approach to reduce such imperfections is to measure PAD images with LCP and RCP light from one enantiomer, followed by the analysis of the PECD image.[10,18,49] If the laser propagation is along the z-axis of a Cartesian coordinate system and the spectrometer axis is parallel to the x-direction (see Figure 1 and 2), the PECD image (PECD(y,z)) is [Eq. (2)]:

$$\text{PECD}_{(en)}(y,z) = I^{LCP}_{(en)}(y,z) - I^{RCP}_{(en)}(y,z) \qquad (2)$$

where (en) denotes a given enantiomer (en$=+/-$) and will be omitted if not explicitly necessary. The sign $(+)$ or $(-)$ refers to the optical activity of the enantiomer used. $I(y,z)$ is the PAD image, that is, the projection of the three-dimensional momentum distribution resp. electron density [see Figure 1 and Eq. (5)], for a given helicity. The PECD images resulting from both enantiomers are mirror images of one another (with the y-axis as the mirror axis): PECD$_{(+)}(y,z) =$ PECD$_{(-)}(y,-z)$.

The measured PAD images can be decomposed into a gerade (g) and ungerade (u) part $I(y,z) = I_g(y,z) + I_u(y,z)$, defined by $I_g(y,-z) = I_g(y,z)$ and $I_u(y,-z) = -I_u(y,z)$. Due to parity conservation (see above), a change in the helicity of the photon or an exchange of the enantiomer implies a change of sign only in the ungerade part: $I^{LCP}_{(u)}(y,z) = -I^{RCP}_{(u)}(y,z)$ or $I^{LCP}_{(+,u)}(y,z) = -I^{LCP}_{(-,u)}(y,z)$. Due to the cancellation of the gerade part $I_g(y,z)$ it follows from Equation (2) that an ideal PECD image exhibits a pure antisymmetric character [Eq. (3)]:

$$\text{PECD}(y,z) = 2I^{LCP}_u(y,z) \qquad (3)$$

Note that the decomposition operation is linear. It can also be executed on the PECD images. In an ideal experiment the PECD image of one specific enantiomer possesses no gerade part, that is, PECD$_g(y,z) = 0$ and therefore PECD(y,z) = PECD$_u(y,z)$. Thus, for a real experiment one should consider the antisymmetric part of a PECD image [PECD$_u(y,z)$]. Remaining imperfections can be significantly reduced further by applying the difference of the PECD images (ΔPECD) of both enantiomers[22,37] [Eq. (4)]:

$$\begin{aligned}\Delta\text{PECD} &= \text{PECD}_{(+)}(y,z) - \text{PECD}_{(-)}(y,z) \\ &= 2\text{PECD}_{(+,u)}(y,z) = 4I^{LCP}_{(+,u)}(y,z)\end{aligned} \qquad (4)$$

In the following, the PECD effect will be discussed in terms of the properties of the relevant physical quantity, that is, the three-dimensional photoelectron (momentum) distribution which is described by the electron density $\rho(x,y,z)$, see Figure 1. Consider the ionization of randomly oriented molecules using
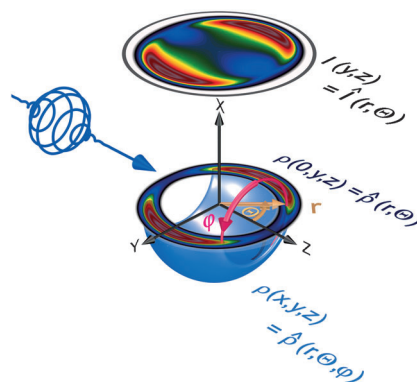
Figure 1. Measured PAD image $I(y,z) = \hat{I}(r,\Theta)$, resulting from an Abel transformation of the PAD, namely the photoelectron density $\rho(x,y,z) = \hat{\rho}(r,\Theta,\varphi)$ corresponding to a three-dimensional momentum distribution and cut through the density $\rho(0,y,z) = \hat{\rho}(r,\Theta)$, that is, the Abel-inverted image.

circularly polarized light propagating along the z-direction $\vec{k}\|\vec{z}$. r is the radial distance from the origin, related to the excess energy of the photoelectrons. As introduced above, Θ is the polar angle between the electron emission and the laser pulse propagation direction. φ is the azimuthal angle about the z-axis. Since the density $\rho(x,y,z) = \hat{\rho}(r,\Theta,\varphi)$ is cylindrically symmetric, that is, independent of φ, we can restrict the considerations to $\rho(0,y,z) = \hat{\rho}(r,\Theta)$, which is described by Equation (8), where the angular distribution $P(\Theta)$ was introduced in Equation (1). Although $\rho(x,y,z)$ and $\hat{\rho}(r,\Theta,\varphi)$ describe the same density using different coordinates, we emphasize by the notation that they are represented by different mathematical functions.

In a VMI set-up, the emitted photoelectron distribution is Abel-transformed (A) onto a detector surface. Therefore, the measured PAD image $I(y,z)$ is described by integration of $\rho(x,y,z)$ along the x-axis [Eq. (5)]:

$$I(y,z) = \int_{-\infty}^{\infty} \rho(x,y,z)dx \qquad (5)$$

By applying the inverse Abel transformation (A^{-1}) on the measured PAD image $I(y,z)$, a section through the initial distribution at $x=0$ is obtained, that is, the Abel-inverted image $\rho(0,y,z) = \hat{\rho}(r,\Theta) = A^{-1}I(y,z)$. Integration over the whole distribution yields the total photoelectron signal T [Eqs. (6)]:

$$T = \int_{-\infty}^{\infty}\int_{-\infty}^{\infty}\int_{-\infty}^{\infty} \rho(x,y,z)\,dx\,dy\,dz$$

$$= \int_{-\infty}^{\infty}\int_{-\infty}^{\infty} I(y,z)\,dy\,dz \tag{6a}$$

$$= 2\pi \int_0^{\pi}\int_0^{\infty} \hat{\rho}(r,\Theta)r^2 \sin(\Theta)\,dr\,d\Theta \tag{6b}$$

This integration can either be performed by two-dimensional integration over the PAD image [Eq. (6a)] or integration over the Abel-inverted image [Eq. (6b)]. For measured PECD effects, asymmetries are expected to arise with respect to the light propagation. Therefore the total signals in forward direction (F) and backward direction (B) have to be considered. These total signals can be obtained from Equation (6) via integration over the respective hemisphere. Again, the integrations can be executed equivalently, using the Abel-inverted image or the PAD image [Eq. (7)]:

$$F = 2\pi \int_0^{\pi/2}\int_0^{\infty} \hat{\rho}(r,\Theta)r^2 \sin(\Theta)\,dr\,d\Theta$$

$$= \int_0^{\infty}\int_{-\infty}^{\infty} I(y,z)\,dy\,dz$$

$$B = 2\pi \int_{\pi/2}^{\pi}\int_0^{\infty} \hat{\rho}(r,\Theta)r^2 \sin(\Theta)\,dr\,d\Theta \tag{7}$$

$$= \int_{-\infty}^{0}\int_{-\infty}^{\infty} I(y,z)\,dy\,dz$$

For the subsequent discussion we assume that the Abel-inverted image $\hat{\rho}(r,\Theta)$ can be separated into a radial part $f(r)$ and an angular part $P(\Theta)$ [Eq. (8)]:

$$\hat{\rho}(r,\Theta) = f(r)P(\Theta) \tag{8}$$

This separation is justified if the photoelectrons originate from a single ionization channel or from ionization channels that are sufficiently separated in the kinetic energy of the electrons.

Since the Legendre polynomials are ungerade functions for odd values of l and gerade functions for even values of l, the Abel-inverted image $\hat{\rho}(r,\Theta)$ can be decomposed into its ungerade and gerade contributions in the following way [Eq. (9)]:

$$\hat{\rho}(r,\Theta) = \hat{\rho}_g(r,\Theta) + \hat{\rho}_u(r,\Theta)$$

$$= f(r)\left(\sum_{l_{even}} c_l P_l[\cos(\Theta)] + \sum_{l_{odd}} c_l P_l[\cos(\Theta)]\right) \tag{9}$$

The symmetry properties of the Legendre polynomials $P_l[\cos(\Theta)]$ are considered with respect to $\Theta = \pi/2$ because the function $\cos(\Theta)$ is ungerade with respect to this angle. In the PAD images, this corresponds to the symmetry in forward

[$\Theta \in (0,\pi/2)$ or $z > 0$] and backward [$\Theta \in (\pi/2,\pi)$ or $z < 0$] direction, that is, with y-axis being the mirror axis.

Whereas for the detailed comparison to theory knowledge about the individual amplitudes of all contributing Legendre polynomials is required, for many practical applications a quantification of the PECD images with a single number would be desirable.

A straightforward method is based on an extension of one-photon PECD quantifications.[10] In the one-photon ionization case the PECD effect has been quantified by taking twice the difference between forward and backward emission of the photoelectrons normalized to the mean intensity per hemisphere, that is, half of the total signal.[10] The factor two arises because in the one-photon case the maximum effect is observed in the exact forward and backward direction ($\Theta = 0°$ and $180°$). This measure has been extended to the multiphoton case.[37,38] We refer to those definitions and define the linear PECD (LPECD) in the same way as $\text{LPECD} = \frac{2(F-B)}{T/2}$. To evaluate this measure we start by expressing the total signal defined in Equation (6) in terms of Legendre coefficients using Equations (8) and (1), as shown in Equation (10):

$$T = 2\pi \int_0^{\infty} f(r)r^2 dr \int_0^{\pi} P(\Theta)\sin(\Theta)\,d\Theta$$

$$= 2\pi R \sum_l c_l \int_0^{\pi} P_l[\cos(\Theta)]\sin(\Theta)\,d\Theta \tag{10}$$

$$= 4\pi R c_0$$

where R is defined as the radially integrated signal $R = \int_0^{\infty} f(r)r^2 dr$. Note that only c_0 determines the total signal. In the same way it follows for the total signal in forward direction, as shown in Equation (11) [also see Eq. (7)]:

$$F = 2\pi R\left(c_0 + \sum_{l_{odd}} p_l c_l\right) = 2\pi R(c_0 + s_{odd}) \tag{11}$$

and analogously for the backward direction, as shown in Equation (12):

$$B = 2\pi R(c_0 - s_{odd}) \tag{12}$$

where the weights p_l in the sum are obtained analytically by Equation (13):

$$p_l = \int_0^{\frac{\pi}{2}} P_l[\cos(\Theta)]\sin(\Theta)\,d\Theta$$

$$= \begin{cases} 1 & \text{for } l = 0 \\ 0 & \text{for even } l > 0 \\ (-1)^{\frac{l-1}{2}}\frac{l!!}{l(l+1)(l-1)!!} & \text{for odd } l \end{cases} \tag{13}$$

and $s_{odd} = \sum_{l_{odd}} p_l c_l$ is introduced as a short-hand notation. A decomposition of F and B into gerade and ungerade components results in Equation (14):

$$F_g = 2\pi R c_0 = \frac{T}{2} = \int_0^\infty \int_{-\infty}^\infty I_g(y,z)\, dy\, dz = B_g = \frac{1}{2}(F+B) \tag{14}$$

and Equation (15):

$$F_u = 2\pi R s_{odd} = \int_0^\infty \int_{-\infty}^\infty I_u(y,z)\, dy\, dz = -B_u = \frac{1}{2}(F-B)$$
$$= \frac{1}{2}\int_0^\infty \int_{-\infty}^\infty PECD_u(y,z)\, dy\, dz \tag{15}$$

As introduced above, we can now write for the LPECD [Eq. (16)]:

$$LPECD = \frac{2(F-B)}{T/2} = \frac{8F_u}{T} = \frac{4s_{odd}}{c_0}$$
$$= \frac{4\int_0^\infty \int_{-\infty}^\infty PECD_u(y,z)\, dy\, dz}{\frac{1}{2}\int_{-\infty}^\infty \int_{-\infty}^\infty [I^{LCP}(y,z) + I^{RCP}(y,z)]\, dy\, dz} \tag{16}$$

From an experimental view it is equivalent to use $LPECD = 4\frac{F_{PECD} - B_{PECD}}{T^{LCP} + T^{RCP}}$, where F_{PECD} (B_{PECD}) describes the PECD in forward (backward) direction.

Thus, it can also be derived from the experimentally obtained ungerade part of the PECD image that is, $PECD_u(y,z)$. As the measured PAD images $I(y,z)$ and the $PECD_u(y,z)$ are related to the Abel inversion, Equation (16) can also be expressed by the coefficients of the Legendre polynomials (see above) [Eq. (17)]:

$$LPECD = \frac{1}{c_0}\left(2c_1 - \frac{1}{2}c_3 + \frac{1}{4}c_5 - \frac{5}{32}c_7 + \ldots\right)$$
$$= \frac{4}{c_0}\sum_{l_{odd}} p_l c_l \tag{17}$$

where c_l are the amplitudes of the contributing Legendre polynomials in the angular part, see Equation (1). In contrast to one-photon ionization, where Equation (17) reduces to $LPECD_{1\hbar\omega} = 2c_1/c_0$,[10] higher-order modulations, that is, higher orders of odd coefficients result in the multiphoton case. In cases where the odd coefficients in the alternating sum in Equation (17) change sign, the absolute value of the LPECD is maximized when higher-order odd components are taken into account. Such behaviour could be rationalized, as multiphoton ionization with light of a given helicity is expected to increase the overall asymmetry. This behaviour is nicely reflected in the data (see Tables 2 and 4).

However, this LPECD may not be a suitable criterion to quantify chiral effects in general as this quantity can become zero if the signals F and B are the same although the PAD images are different for the two enantiomers. If expressed in terms of the amplitudes in the contributing Legendre polynomials, this will correspond to a case where the alternating sum of the odd coefficients in Equation (17) becomes zero. This might happen due to the nature of possibly involved different ionization processes in multiphoton excitation and ionization

schemes or due to the contribution of different conformers[54] [see also comment to Eq. (8)].

In order to avoid the abovementioned cancellation effects we propose two further methods based on the analysis of gerade and ungerade contributions to the PAD.

In a first approach we decompose the Abel-inverted image $\hat{\rho}(r,\Theta)$ into its gerade and ungerade part according to Equation (9). We then analyse the square root applied to the ratio of the integral of the squared ungerade part $\hat{\rho}_u^2(r,\Theta)$ and the square of the full Abel-inverted image $\hat{\rho}^2(r,\Theta)$ as a measure for the circular dichroism. We define the total signal for the ungerade contribution as Equation (18):

$$\mathcal{U}^2 = \int_0^{2\pi}\int_0^\pi\int_0^\infty [\hat{\rho}_u(r,\Theta)]^2 r^2 \sin(\Theta)\, dr\, d\Theta\, d\varphi$$
$$= 2\pi\int_0^\infty [f(r)]^2 r^2 dr \int_0^\pi [P_u(\Theta)]^2 \sin(\Theta)\, d\Theta$$
$$= 2\pi\mathcal{R}^2 \int_0^\pi [P_u(\Theta)]^2 \sin(\Theta)\, d\theta = 2\pi\mathcal{R}^2 \sum_{l_{odd}} \frac{2}{2l+1}c_l^2 \tag{18}$$

where
$[P_u(\Theta)]^2 = \left\{\sum_{l_{odd}} P_l[\cos\Theta]\right\}^2 = \sum_{l_{odd}}\sum_{l_{odd}} c_l P_l[\cos\Theta]c_{l'}P_{l'}[\cos\Theta]$. Due to the orthogonality of the Legendre polynomials, $\int_0^\pi P_l[\cos(\Theta)]P_{l'}[\cos(\Theta)]\sin(\Theta)\, d\Theta = \frac{2}{2l+1}\delta_{ll'}$ was used to evaluate the angular integral and the radial integral is defined as $\mathcal{R}^2 = \int_0^\infty [f(r)]^2 r^2 dr$. Hence, the expression for the squared ungerade part and analogously for the gerade signal and the total signal is given by Equations (19) and (20):

$$\mathcal{U}^2 = 2\pi\mathcal{R}^2 \sum_{l_{odd}} \frac{2}{2l+1}c_l^2 \tag{19}$$

$$\mathcal{G}^2 = 2\pi\mathcal{R}^2 \sum_{l_{even}} \frac{2}{2l+1}c_l^2 \tag{20}$$

and Equation (21):

$$\mathcal{T}^2 = \mathcal{U}^2 + \mathcal{G}^2 = 2\pi\mathcal{R}^2 \sum_{l=0}^{2n} \frac{2}{2l+1}c_l^2 \tag{21}$$

With regard to the Legendre coefficients we obtain a quadratic PECD (QPECD) measure as Equation (22):

$$QPECD = \sqrt{12}\frac{\mathcal{U}}{\mathcal{T}} = \sqrt{12}\sqrt{\frac{\sum_{l_{odd}}\frac{c_l^2}{2l+1}}{\sum_{l=0}^{2n}\frac{c_l^2}{2l+1}}}$$
$$\approx \frac{\sqrt{12}}{c_0}\sqrt{\sum_{l_{odd}}\frac{c_l^2}{2l+1}} \tag{22}$$

where the factor $\sqrt{12}$ is introduced to enable agreement with the LPECD for the single-photon case. In addition, the denominator in Equation (22) was simplified by taking the weight factors of $\frac{1}{2l+1}$ into account, as the proportion of c_0 is greater than all the other contributions in the denominator.

This QPECD measure cannot be extracted directly from the measured data. An Abel inversion is required to obtain the

Legendre coefficients and to calculate the QPECD. Therefore, a second, more practical method can be justified in the following way: in many cases an Abel inversion or a distinct assignment of Legendre coefficients cannot be performed due to lack of symmetries, for example, when elliptically polarized light is used. A pure summation over the total PECD$_u$ image will return zero due to the antisymmetric character. Thus, analogously to the motivation of the abovementioned method, in order to avoid undesired cancellation effects, we suggest evaluating the power PECD measure (PPECD) as the square root of the ratio of the integrated squared antisymmetric PECD image and the total squared signal [Eq. (23)]:

$$PPECD = 4\sqrt{\frac{\int_{-\infty}^{\infty}\int_{-\infty}^{\infty}\{PECD_u(y,z)\}^2\, dy\, dz}{\int_{-\infty}^{\infty}\int_{-\infty}^{\infty}\{I^{LCP}(y,z) + I^{RCP}(y,z)\}^2\, dy\, dz}} \qquad (23)$$

An additional factor of two was introduced to obtain similar values as in the case of LPECD and QPECD in the limit of one-photon ionization. Note that all defined quantities belong to different normalization procedures regarding the total signal when expressed in %.

The three different measures will be applied to our experimental results on camphor, fenchone and norcamphor.
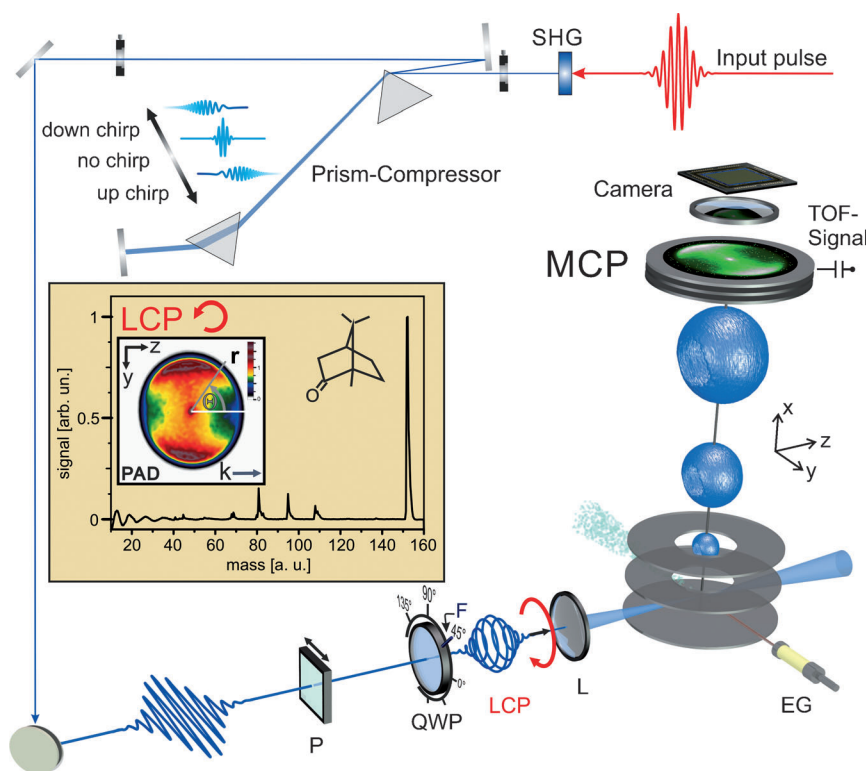
Experimental Section

The experimental set-up is sketched in Figure 2. Femtosecond laser pulses of 25 fs pulse duration [full width at half maximum (FWHM) of the intensity] at a central wavelength of 795 nm and a pulse energy of 800 μJ are provided by an amplified 1 kHz Ti:sapphire laser system (Femtolasers Femtopower Pro). A nonlinear crystal (β-BBO, 100 μm thickness, Dayoptics, Inc.) is used to generate the second harmonic (SHG). The SHG laser pulses, centred at 398 nm, have approximately a Gaussian shape and a spectral width of 9 nm. A prism compressor realized in a double-pass configuration consisting of two fused silica prisms is used for the dispersion compensation of the SHG laser pulses.[55] In situ dispersion compensation is achieved by maximization of the multiphoton ionization of Xenon atoms. Assuming a Gaussian temporal profile, we estimate a bandwidth limited pulse duration of 25 fs in the interaction region. The laser beam is focussed with a lens of 200 mm focal length into the spectrometer and intersected with the specimen beam provided by an effusive gas inlet. The laser focus was measured with a beam profiling CCD camera (WinCamD, DataRay Inc.). A mean focal spot size radius of about 40 μm (1/e^2 of intensity profile) was obtained. At 2.5 μJ pulse energy this leads to a peak intensity of about $I_0 = 4 \times 10^{12}$ W cm^{-2} assuming Gaussian profiles in time and space. The peak intensity is also in accordance with measured ponderomotive shifts observed in the ionization of Xenon atoms at the given conditions (see Section 3.1.3. and Figure 10). At I_0 the Keldysh γ parameter for a small chiral molecule with an IP in the range of 10 eV $\pm$ 2 eV is larger than eight, hinting to a multiphoton regime.

A continuous gas flow to the interaction region is provided via the effusive gas inlet. This inlet ends with a copper tube of 0.3 mm inner diameter. It is placed 5 mm in front of the laser focus, perpendicular to the laser beam and perpendicular to the spectrometer axis. The chiral substances are filled in glass cylinders embedded in a heatable water bath outside the vacuum chamber. The complete effusive gas inlet is heated exceeding 60 °C to avoid condensation. Typical chamber pressures during measurements were in the order of 10^{-6} mbar. A home-built

Figure 2. Experimental set-up with beam path and imaging spectrometer: Femtosecond laser pulses at 1 kHz repetition rate are frequency doubled in a nonlinear crystal to achieve pulses centred around 398 nm (SHG). A prism compressor is used for *dispersion compensation*, in situ in the interaction region of the focused laser beam (L: lens) and a specimen beam from an effusive gas inlet (EG). A pulse duration of approximately 25 fs and a pulse energy of 2.5 μJ result in a peak intensity I_0 of about 4×10^{12} W cm^{-2}. The quarter-wave plate (QWP) converts linearly polarized (LIN) laser pulses (P: polarizer) for instance into left circular (LCP) or right circular polarization (RCP). Dependent on the angle between the fast axis (F) and the polarization axis of the incoming light, elliptical polarization of different helicity is obtained. The spectrometer is used to record images $I(y,z)$ of projections of three-dimensional photoelectron angular distributions (PADs) via an imaging multi-channel plate assembly (MCP) and a CCD camera. Alternatively ion time-of-flight (TOF) mass spectra are recorded via a capacitive coupled output. The inset shows for (S)-(−)-camphor using LCP light a typical ion TOF spectrum with little fragmentation (parent ion at 152 u) and the corresponding PAD image [$I^{LCP}_{(−)}(y,z)$]. For the PAD image the angle of the photoelectron emission Θ is measured with respect to the propagation direction of the light. The radius r is proportional to the square root of the excess energy.

spectrometer[31] is used either to record PAD images $I(y,z)$ in VMI[56] mode or, by changing the polarity of the electrostatic lens, to measure mass spectra in Wiley-McLaren[57] time-of-flight (TOF) mode. The imaging detector (SI-Instruments GmbH model S3075-10-I60-PS-FM, 75 mm effective diameter) consists of two microchannel plates (MCP) in a Chevron configuration with a phosphor screen deposited on a fiber optic. The signals on the phosphor screen are imaged with a 1.4 million pixel 10 bit CCD-camera (Lumenera Corporation model Lw165m). As introduced in Section 2, the obtained PAD images $I(y,z)$ are Abel-projected (A) three-dimensional PADs $\rho(x,y,z)$ and are given in the following as a function of radius r and angle Θ. In an Abel-inverted image the velocity of the photoelectrons, and therefore the corresponding radius r, increases from the centre of the distribution to the edge and is proportional to the square root of the excess energy. For energy calibration or equivalently momentum calibration of the VMI spectrometer we use the third harmonic of a nanosecond Nd:YAG laser at 355 nm to ionize Xenon atoms in a 3+1 REMPI process. The corresponding PADs in the (Xe II $^2P_{3/2}$ and Xe II $^2P_{1/2}$) continua are not ponderomotively shifted[58] by the nanosecond laser pulses and are therefore well-defined in energy.[59] The radius-to-energy calibration is performed on the Abel-inverted data. Using the mentioned Nd:YAG laser, additional calibration energies were obtained from ionization of residual water and five-photon ionization of krypton (Kr II $^2P_{3/2}$ and Kr II $^2P_{1/2}$). Taking the zero-energy photoelectrons at the centre of the image into account, we obtained six calibration points from 0 eV to 3.5 eV. The measured resolution for the spectrometer settings used in the presented measurement is better than 80 meV FWHM at an energy of about 0.5 eV. Signals from time-of-flight mass spectra (TOF-MS) are extracted via a capacitive coupled output from the high-voltage power supply of the phosphor included in the imaging-assembly (indicated in Figure 2) and are recorded using a digital oscilloscope (Teledyne LeCroy model LC564DL) with a time resolution of 0.5 ns. The TOF-MS are calibrated with the help of the Xenon isotopes and a signal from residual water. The achieved mass resolution $m/\Delta m$ is about 250.

Initially, the polarization of the incoming SHG light is LIN with the polarization axis perpendicular to the spectrometer axis and thus coplanar to the detector surface. To clean up the linear polarization further we use a dichroitic UV polarizer (CODIXX). An achromatic quarter-wave plate (QWP) (B. Halle Nachfl.) generates either left (LCP) or right circularly polarized (RCP) light, if the fast axis is adjusted 45° or 135°, respectively, to the polarization axis. In the experiment, this angle is measured looking in the direction of the laser propagation in a mathematically positive sense (see Figure 2). All other angles between the fast axis and the polarization axis result in elliptically or linearly polarized light. A referenced QWP (B. Halle Nachfl.) was used to confirm the direction of the fast axis. The helicity and the handedness of the light is assigned using the optical convention,[60] where Powis suggested to use this convention also for PECD studies.[18] In this convention the light is defined by the rotation of the electric field vector with time looking towards the light source. A clockwise direction is termed RCP light. The degree of polarization is determined by using an additional polarizer after the QWP measuring the transmitted laser intensity. For instance, at LCP and RCP the resulting curves show the same shape (see Figure 7 third row right image). The derived value of the Stokes S_3 parameter[60–62] is $|S_3| = 99\%$ (further details are given in the Supporting Information SI4). No net stress-induced birefringence was observed through the laser entrance and exit window of the vacuum chamber. Nevertheless, a contribution in the interaction region cannot be excluded.

In the measurements, the PAD images are recorded using different polarizations of the ionizing laser pulses for example, LIN, LCP, RCP

or a certain elliptical polarization. In the presented PAD images the laser propagation direction is always from left to right (see Figure 2). Potential small drifts in the set-up, such as laser intensity fluctuations and pressure variations may result in an undesired offset that could arise when two PAD images are compared by subtracting them. To minimize such effects, a stepper motor is used to rotate the QWP to switch between two subsequent measurements of the desired polarizations, for example, LCP and RCP, back and forth 50 times. A measurement of two PAD images with different polarizations takes around 15 min for the data presented in this contribution and contains an average of about 300 000 laser pulses. The related electron-count statistics for one PAD measurement are dependent on the studied specimen and therefore on the ionization process. Such statistics are presented as an example in the discussion of our results on camphor.

Before evaluation and with respect to the arbitrary signal levels from the CCD camera, each recorded PAD image $I_{raw}(y,z)$ is normalized after smoothing by the averaged signal T [corresponding to Eq. (6)]. Photoelectrons below 0.02 eV have not been considered for this normalization because they seem to stem from other ionization processes (see Section 3.1.3.). However, the normalization is not significantly influenced by omitting these low-energy photoelectrons. In order to facilitate visual comparison of data sets from different substances one additional scaling factor s_{subst} for each substance was applied on $I^{LIN}(y,z)$, $I^{LCP}(y,z)$ and $I^{RCP}(y,z)$ such that the signal height at FWHM corresponds to unity in the colour coding. $I(y,z) = \frac{1}{T} s_{subst} I_{raw}(y,z)$, for the bicyclic ketones that is, $s_{camphor} = 0.67$, $s_{fenchone} = 0.67$ and $s_{norcamphor} = 0.91$. This scaling factor is irrelevant for the following quantitative analysis. Additional factors (that are not used for the quantitative analysis given below) to compare PAD images from linearly and circularly polarized light on one colour scale are given Figures 3 and 4.
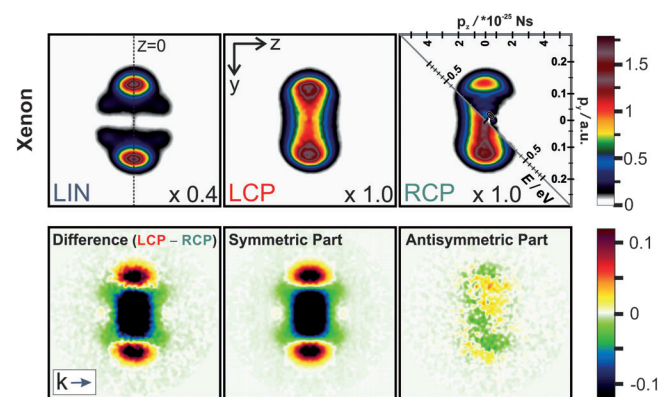
In general, the ionization pathways in a REMPI experiment and hence the shape of the three-dimensional PAD is dependent on the polarization. This was demonstrated with the creation and tomographic reconstruction of designer electron wave packets resulting from REMPI of potassium atoms with polarization-shaped laser pulses.[31,33,34] In the experiment presented here LIN, LCP and RCP light is used as well as elliptically polarized light. As mentioned in Section 2, for LIN the free-photoelectron wave packets are cylindrically symmetric with respect to the laser polarization. In the case of LCP or RCP, the free-photoelectron wave packets also possess such a cylindrical symmetry, but with respect to the laser propagation direction (k-vector) (see Figure 2). These are the polarization states where an Abel inversion can be performed. This inverse Abel transformation can be used to obtain a slice through the equatorial plane of the PAD, that is, the Abel-inverted image. In our geometry, this slice is both parallel to the detector plane and coplanar to the k-vector (see Figure 1). It includes all necessary information about the initial three-dimensional object, for example, the excess energies, and especially the angular distributions according to Equation (1) and detailed in Section 2. To extract that information we use an adapted version of the pBasex-algorithm.[53] As the observed PAD images exhibit no sharp features, they are downscaled from 1.4 million pixel and polarly mapped in one operation to 180×200 pixel (angle Θ and radius r with an angular step size of $\Delta\Theta = 2°$) before execution of the pBasex. For symmetry reasons, the pBasex is performed only on one half-sphere of the PAD image, making use of the average of the upper and lower half-spheres, that is, performing a symmetrization with respect to the k-vector. The pBasex algorithm delivers an Abel-inverted density expanded into a sum of Gaussian distributions modulated by Legendre polynomials as described in Equation (24). We used 100 spherical Gaussian distributions with their centre points r_k in

steps of 2 pixel. Each Gaussian has a width σ of 2 pixel and is multiplied by a sum of 4 even and 4 odd Legendre polynomials. Higher-order Legendre polynomials are additionally considered, but do not contribute significantly. Note that from the general considerations given above concerning a three-photon process, the decomposition into 3 even and 3 odd components should be sufficient. We decided to include higher orders for an unbiased data evaluation.

$$\hat{\rho}(r,\Theta) = \sum_{k,l=0}^{k=100,l=8} c_{kl} e^{-\frac{(r-r_k)^2}{\sigma}} P_l(\cos\Theta) \tag{24}$$

The offset for each radial set of coefficients is determined by the coefficient of the zero-order Legendre polynomial c_{k0}. The coefficients c_{kl} of each radius r_k and the different orders l of the corresponding Legendre polynomials are obtained from the pBasex algorithm. Using these coefficients, a radial dependent weighting $\bar{c}_{kl} = c_{kl} r_k^2$ was applied in order to reconstruct the initial three-dimensional density [see also Eq. (6b) and Ref. [53]].

Before we proceed with our results on chiral molecules, we present the experimental procedure on achiral Xenon atoms. First we minimized residual asymmetries in the projection of the PADs onto the detector surface, which are not related to the polarization of the light. To that end, we recorded images from multiphoton ionization of Xenon with 398 nm LIN light and compensated perturbing magnetic fields with the help of Helmholtz coils surrounding our spectrometer to yield symmetric PAD images (see Figure 3 top row, left image). The measured PAD images for LIN, LCP and RCP light at 1.8 I_0 are also shown in Figure 3. The total PAD signal T of the LIN-PAD image is approx. 50% higher than the total signals from the LCP- and RCP-PAD images, also in accordance with the integrated TOF signals. Regarding the ionization with LIN, the PAD image [$I^{LIN}(y,z)$] exhibits contributions with p- and f-type symmetries (see also Ref. [63,64]). A mirror axis can be chosen through the centre of the PAD image coinciding with the direction of the linear polarization (see Figure 3). Ionization with LCP or RCP light results in toroidally shaped structures that are also symmetric. After the absorption of four photons, the excess energy of the electron distributions originating from ionization into the lower fine structure Xe II $^2P_{3/2}$ state[65] is expected to be at approximately 0.33 eV. In our measurements at 1.8 I_0, this excess energy peaks at ≈ 0.25 eV. This energy difference of about 80 meV is attributed to a ponderomotive shift of the ionization potential[58] and confirms the determination of our I_0 (see also Figure 10). A consistent ponderomotive shift was observed in a range from 0.5 I_0 up to 3 I_0. The difference image of the PAD images [$I^{LCP}(y,z) - I^{RCP}(y,z)$] is shown in the left lower row of Figure 3. This difference corresponds to the PECD as described in Equation (2). The PECD image of Xenon shows a symmetrical shape with respect to the indicated mirror axis in Figure 3. A decomposition of the PECD image [PECD(y,z)] in its symmetric and antisymmetric part [PECD$_g(y,z)$, PECD$_u(y,z)$] was performed by 180° back-folding along the z-axis as well as with respect to the mirror axis perpendicular to it. The antisymmetric part was obtained by subtracting the symmetrized part from the original PECD image. There are no structured antisymmetric components visible as expected and the PECD is dominated by the symmetrical contributions that are attributed to residual optical imperfections of our set-up.

3. Results and Discussion

So far, we have demonstrated on achiral Xenon atoms that our experimental set-up is not creating structured antisymmetric components in a typical PECD experiment. We now proceed to give a detailed account of the quantification of the experimental multiphoton PECD, taking the camphor molecule as a prototype. To that end, we initially describe the raw images obtained with LIN, LCP and RCP light. Secondly, we discuss PECD and ΔPECD on the raw data as well as on Abel-inverted data sets. We quantify these results with respect to the three measures introduced in Section 2 and end this section by analysing the PECD with elliptically polarized light. In the latter case, only the *power PECD* can be applied for quantification. In addition to that, we use our tomographic reconstruction method to obtain a three-dimensional PECD. We show that for circularly polarized light this method delivers similar odd Legendre coefficients as compared to the Abel inversion and discuss results from elliptical polarization where due to a lack of symmetry an Abel-inversion is not possible. In order to study the role of an intermediate resonance and possible origins of the PECD effect, we investigate intensity-dependent measurements. The results reveal dissociative ionization as the origin of the observed PECD effect, whereas ionization of the intermediate resonance is dominating the signal. After gathering all this information, we compare the quantification results on camphor of this contribution with our previous contribution[22] and with recently published data from Janssen and co-workers.[37] Finally, we present and discuss our PECD results obtained from the family of the bicyclic ketones, that is, camphor, fenchone and norcamphor. At the end, a comparison of the PECD on an

Figure 3. PAD images [$I(y,z)$] of xenon, ionized with 398 nm laser pulses at a peak intensity of 1.8 I_0. Upper row: Ionization with LIN, LCP and RCP light, respectively. The energy distribution corresponds to the Xe II $^2P_{3/2}$ ionic state and peaks at approx. 0.24 eV. The laser propagation k is from left to right, as indicated by an arrow. A scaling factor of 0.4 is used for the colour scale of the LIN-PAD image for comparison with the less intense LCP- or RCP-PAD images (see text). The image above the diagonal to the RCP-PAD image shows the Abel-inverted image with calibrated scales of energy and momentum. For convenience the p_z and p_y axis are given in SI units and atomic units, respectively. Lower row: Difference signal of the PAD images measured with circularly polarized light by taking the LCP-PAD image minus RCP-PAD image [PECD(y,z)] and decomposition in its symmetric and antisymmetric part [PECD$_g(y,z)$, PECD$_u(y,z)$], derived via 180° back-folding (along the z-axis as well as with respect to the mirror axis perpendicular to it, shown by the dashed line in the middle image). The PECD image of xenon appears without any structured antisymmetric components with respect to the mirror axis [chosen that $I(y,z) = I(y,-z)$, dashed line]. Remaining symmetrical parts in the difference could be due to residual optical imperfections of our set-up.
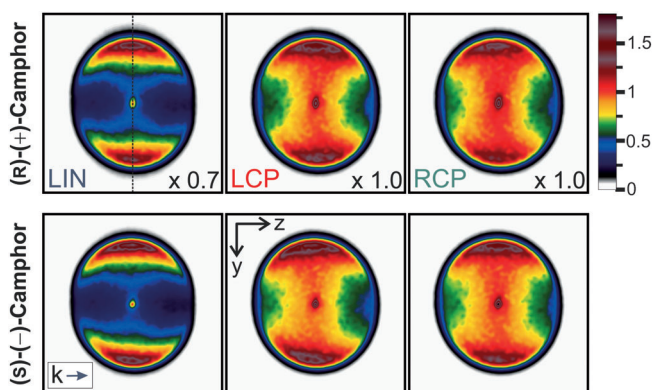
enantiomer of norcamphor to the PECD of a racemic mixture will be presented, hinting at the analytical sensitivity that could be obtained in the future.

3.1. Quantification of Multiphoton PECD on the Camphor Prototype

Details of the chemical sample and the excitation scheme are given in the next section together with the analysis of the other bicyclic Ketones. The PAD images from camphor after three-photon ionization with 398 nm laser pulses at a peak intensity of I_0 are shown in Figure 4. For every laser pulse we measured approximately 50 photoelectrons at I_0. Each PAD image (see Figure 4) contains an average of about 300 000 laser pulses and comprises an electron count in the 10^7 range. They are mainly concentrated at the excess energy. We therefore neglect errors based on counting statistics.

From ionization with LIN light, the PAD images of (R)-($+$)-camphor and (S)-($-$)-camphor are symmetrical with respect to the laser propagation, defined by $\vec{k}$. The corresponding mirror axis (see Figure 4) is perpendicular to it. These PAD images do not exhibit features that can be used to distinguish between both chiral enantiomers. The total PAD signal T of the LIN-PAD image is approx. 15% weaker than the total signals from the LCP- and RCP-PAD images, also matching the integrated TOF signals of the parent ions at comparable fragment-to-ion ratios.

In contrast to the LIN-PAD image, the PAD images, measured with circularly polarized light, reveal signal asymmetries with respe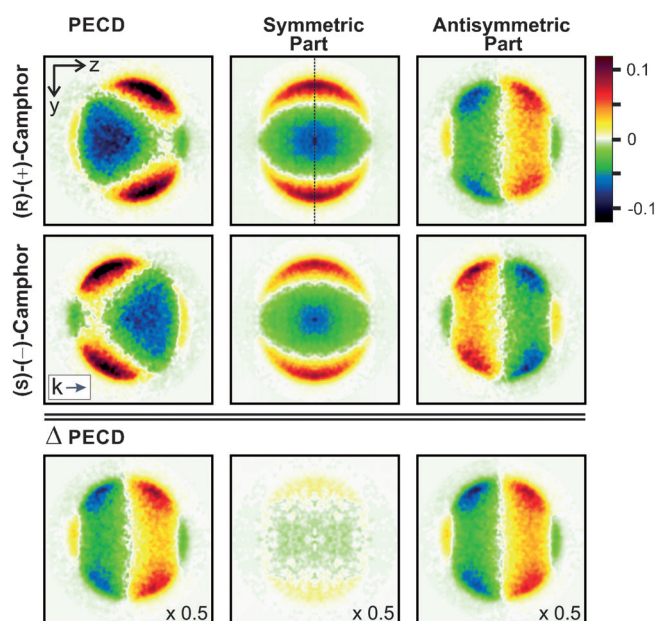ct to the light propagation direction. The PAD image of (R)-($+$)-camphor with LCP light ($I_{(+)}^{LCP}(y,z)$) possesses more signal in the forward direction than in backward direction. The reversed case is found by using RCP light ($I_{(+)}^{RCP}(y,z)$). In this measurement, more signal appears in backward direction than in the forward direction. Changing from (R)-($+$)-camphor to (S)-($-$)-camphor (shown in the second row of Figure 4) and comparing the PAD images for LCP and RCP, ionization with LCP light generates more signal in the backward direction ($I_{(-)}^{LCP}(y,z)$) and RCP light more signal in the forward direction ($I_{(-)}^{RCP}(y,z)$). As mentioned above, these changes, measured in the PAD images by mirroring the helicity of the light or when changing from right-handed to left-handed molecules, that is, mirroring the molecule, are expected from a CD effect. The effect is significantly larger than a conventional CD effect, as it can already be noticed on the raw data. In our investigations on the bicyclic Ketones presented in this contribution, a CD in ionization[4,5] plays only a minor role in comparison to the PECD effect. Such a CD in the absorption would create differences evaluating the integrated TOF signals as well as the total signal of the PAD images by comparing ionization using LCP or RCP light and tends to decrease with increasing intensity (see Ref. [66,67]): For one enantiomer, for example, more signal should be observed on ionization using LCP light. The opposed case, namely more signal on ionization using RCP light, should occur by exchanging the enantiomer. In our measurements, differences in the total PAD signal T for LCP vs. RCP are below 0.2% for (R)-($+$)-camphor and below 0.9% for (S)-($-$)-camphor. However, in the data presented in this contribution the RCP-PAD images deliver slightly more signal for both enantiomers. A small CD in the ionization may be covered by such systematic characteristics of our set-up.

For the used polarizations, the total PAD signals T [see Eq. (6)] for R- and S-camphor differ less than 4% related to inaccuracies in setting the pressures. These differences are mainly covered by the normalization procedure described in the Experimental Section.

In order to analyse the PECD effect, we plot the difference of the PAD images measured with circularly polarized light, that is, the PECD image from camphor. These results are displayed in Figure 5 (see left images of the first two rows). A distinctive asymmetry with respect to the forward/backward direction is detected for both enantiomers. From visual inspection of the colour coding, this asymmetry is roughly in the range of $\pm 10\%$. However, the PECD images are not perfectly antisymmetric. A decomposition into symmetric and antisymmetric parts (shown in Figure 5 middle and right images) is derived via 180° back-folding (see above). The antisymmetric parts [$PECD_u(y,z)$] of (R)-($+$)-camphor and (S)-($-$)-camphor (Figure 5, right images of the first two rows) reveal the expected behaviour of a CD, that is, a change of sign with respect to the laser propagation direction, in case the enantiomer is exchanged (see below). These antisymmetric parts can be expanded by using only odd Legendre polynomials, as these are also antisymmetric with respect to the laser propagation direction (forward/backward direction to the k-vector), see also Equation (9). Comparing both enantiomers, higher-order Legendre polynomials appear and the contribution from the third

Figure 4. PAD images $I(y,z)$ of camphor, ionized with 398 nm laser pulses at a peak intensity of I_0. Upper row: PAD images of (R)-($+$)-camphor resulting from ionization with LIN, LCP and RCP light, respectively [$I_{(+)}^{LIN}(y,z)$, $I_{(+)}^{LCP}(y,z)$ and $I_{(+)}^{RCP}(y,z)$]. The laser propagation as indicated by an arrow is from left to right. A scaling factor of 0.7 is used for the colour scale of the LIN-PAD image for comparison with the LCP- and RCP-PAD images (see text). Ionization with LIN light results in a PAD image that is symmetric with respect to an axis (dashed line) perpendicular to $\vec{k}$ that is, in forward/backward direction such that $I(y,z)=I(y,-z)$. The PAD image obtained with LCP light possesses an asymmetry with respect to the light propagation that is, more signal in forward direction as opposed to the PAD image for RCP light that exhibits more signal in the backward direction. Lower row: PAD images for (S)-($-$)-camphor. Note the change in signal asymmetry in forward/backward direction. Differences in the total PAD signal T for LCP vs. RCP were below 0.2% for (R)-($+$)-camphor and below 0.9% for (S)-($-$)-camphor.

Figure 5. PECD images PECD(y,z) and their decomposition into symmetric and antisymmetric parts for camphor: Top row, left image: PECD image that is, LCP-PAD image minus RCP-PAD image of (R)-(+)-camphor. Middle row, left image: PECD image of (S)-(−)-camphor. On changing the enantiomer, the asymmetry in forward/backward direction is reversed with respect to the laser propagation. Top row, middle and right image: Decomposition of the PECD image of (R)-(+)-camphor into symmetric and antisymmetric part, derived via 180° back-folding (along the z-axis as well as with respect to the mirror axis perpendicular to it, that is, the dashed line in the middle image). Middle row, middle and right image: Same for (S)-(−)-camphor. The antisymmetric parts of (R)-(+)-camphor and (S)-(−)-camphor (right images) are mirror images of one another respectively change sign on changing the enantiomer. The mirror axis (dashed line) is perpendicular to $\vec{k}$. Bottom row: Difference of the PECD images ΔPECD(y,z) from R and S enantiomers (left) and the decomposition into their symmetric part (middle) and antisymmetric part (right). Note that this ΔPECD(y,z) image contains mainly antisymmetric components whereas the remaining residual instrumental symmetric parts are small. For comparison on the same colour scale, the signals of the images in the third row were multiplied by 0.5.

Legendre polynomial dominates the antisymmetric part of the PECD image. Higher orders are expected in this experiment due to the multiphoton nature of the ionization process. The coefficients for the first and third order are of the same order of magnitude but change sign by exchanging the R- with the S-enantiomer. This alteration in the signs of odd polynomials has been observed in one-photon ionization experiments, where the first Legendre polynomial reversed its sign. Even Legendre polynomials are symmetric in this respect and describe the remaining symmetric parts of the PECD images. These symmetric parts are similar in sign and amplitude for both enantiomers and therefore they may be attributed to experimental imperfections (see above). Moreover, they possess the same sign and a comparable amplitude as observed in the difference of the LCP- and RCP-PAD images from Xenon (see Figure 3).

To further remove residual imperfections such as the above-mentioned symmetrical parts, we consider—according to Equation (4)—the ΔPECD(y,z), that is, the difference of the PECD images. The subtraction of the PECD image of the S-enantiomer from the PECD image of the R-enantiomer (see Figure 5 third row, left image) removes these imperfections directly in cases where the enantiomeric purity is similar (see below) or a racemic mixture is used as a reference. The resulting ΔPECD(y,z) consists mainly of antisymmetric components (see Figure 5 third row) that are similar to the PECD$_u$(y,z). This experimental analysis underscores that the PECD effect only appears in the antisymmetric (odd) components of the Legendre polynomials which reverse sign when changing the helicity of the light or the enantiomer.

After this qualitative discussion we now turn to a quantitative analysis of the PECD using our pBasex algorithm. The pBasex algorithm applied to the PAD images retrieves the involved Legendre coefficients of the initial PAD (see the Experimental Section). Because the Abel inversion is a linear operation the algorithm can be either used to invert the LCP- and RCP-PAD images separately or to invert the PECD image directly. Equivalently, it can be executed separately on the symmetric and antisymmetric parts of the decomposed PECD image.

Figure 6 shows the Abel-inverted PECD images [A^{-1}PECD(y,z)] from the data set of (R)-(+)-camphor and (S)-(−)-camphor presented in Figure 5. The distribution in the Abel-inverted PECD images peaks at 0.52 eV excess energy as well as the distributions of the inverted LCP- and RCP-PAD images from Figure 4 (not shown). We therefore restrict our analysis mainly on the FWHM of the energy distribution that is, a range of approx. 0.43–0.66 eV. The retrieved Legendre coefficients c_l^d are an average of the retrieved and weighted $\bar{c}_{kl}$ values (see
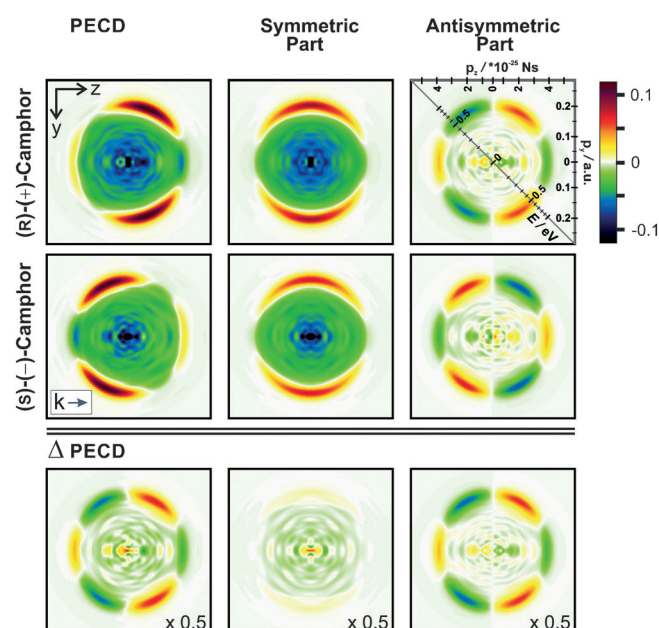
Figure 6. Abel-inverted PECD images A^{-1}PECD(y,z) from the data set of camphor shown in Figure 5. Calibrated scales of energy and momentum are given in the right image in the top row. For convenience the p_z and p_y axes are given in SI units and atomic units respectively. The energy of the observed maximum in the PECD distribution is at about 0.52 eV. The asymmetry in forward/backward direction is visible in the PECD for (R)-(+)-camphor and (S)-(−)-camphor. The A^{-1}ΔPECD(y,z) shows that the symmetric parts cancel where the asymmetric parts add to twice the signal. The values given in Table 1 are averaged over the FWHM of the energy distribution.

the Experimental Section) from the inversion algorithm within the FWHM.

In the following we first extract the coefficients for LCP, RCP, PECD, PECD$_u$, ΔPECD and ΔPECD$_u$ directly from the data of the images in Figures 4 and 5 and present the results in Table 1.

For a check of linearity and the overall performance of our analysis, the coefficients for the PECD and the ΔPECD have additionally been calculated directly from the c_i^d values obtained from LCP and RCP [columns two (R-camphor) and three (S-camphor) in Table 1] and are listed in the Supporting Information SI2 only for completeness as almost the same values were obtained.

Subsequently, in a second step, to obtain representative coefficients for the calculation of quantitative measures (as introduced in Section 2.) and for comparison to theoretical simulations[37,68] (see below), we average the coefficients from ionization with LCP and RCP light (see Table 2).

Table 1 lists the c_i^d values of the retrieved Legendre coefficients from both enantiomers of camphor. The averaged c_i^d values in the cases of LCP, RCP and PECD have been divided by the mean of the averaged zero-order coefficients $\left(c_l^{d,\text{LCP/RCP/PECD}} = \dfrac{\sum_{\text{FWHM}} \bar{c}_{kl}^{\text{LCP/RCP/PECD}}}{\frac{1}{2}\left(\sum_{\text{FWHM}} \bar{c}_{k0}^{\text{LCP}} + \sum_{\text{FWHM}} \bar{c}_{k0}^{\text{RCP}} \right)} \right)$ from ionization with LCP and RCP light. This has been done for each enantiomer separately. For ΔPECD and ΔPECD$_u$, the values are normalized by the mean of the $\bar{c}_{k0}$ coefficients from the $(+)$- and $(-)$-enantiomer $\left(c_l^{d,\Delta\text{PECD}} = \dfrac{\sum_{\text{FWHM}} \bar{c}_{kl}^{\Delta\text{PECD}}}{\frac{1}{4}\left(\sum_{\text{FWHM}} \bar{c}_{k0+}^{\text{LCP}} + \sum_{\text{FWHM}} \bar{c}_{k0+}^{\text{RCP}} + \sum_{\text{FWHM}} \bar{c}_{k0-}^{\text{LCP}} + \sum_{\text{FWHM}} \bar{c}_{k0-}^{\text{RCP}} \right)} \right)$ and multiplied by 0.5 to facilitate comparison. These coefficients are also listed in Table 1.

For the c_i^d values from LCP and RCP (column two and three in Table 1) the significant odd-order components reverse sign

either on changing the helicity of the light or the handedness of the molecule. In contrast, the coefficients of even-order polynomials are nearly identical. Differences in the zero-order coefficients obtained from ionization with LCP ($c_0^{d,\text{LCP}}$) and RCP light ($c_0^{d,\text{RCP}}$) stem from the analysis of the FWHM region. These differences in the retrieved values for c_0 are attributed to small differences in the ellipticity of LCP vs. RCP and remain as symmetric parts in the PECD image. They are not related to the differences in the total signal T of the PAD images, which are below 0.9% and have been already normalized to the same value (see the Experimental Section).

As already visible in the images when going from Figure 4 to Figure 5, taking the difference of both PAD images, that is, creating the PECD image, reduces apparent experimental discrepancies in the c_i^d values as well. Comparing both enantiomers that are measured under the same conditions but are evaluated independently, similar amplitudes for the contributing coefficients are observed in the PECD of R- and S-camphor (left part of columns four and five in Table 1). A clear change in the sign of the odd orders by exchanging the enantiomer is observed up to the fifth order, whereas the third order delivers the main contribution. When analysing the antisymmetric contribution (right part of column four and five in Table 1) the same odd coefficients were obtained. As it is also evident in Figure 5, the symmetric parts as well as the corresponding even coefficients can be reduced significantly by subtracting the PECD images from both enantiomers, that is, the ΔPECD. As a result, the even coefficients possess small amplitudes that are nearly zero and the obtained odd coefficients are the most reliable ones (see column six of Table 1).

In order to obtain representative even and odd coefficients c_l we turn again to the retrieved coefficients listed in Table 1

Legendre polynomial[a]	(R)-$(+)$ camphor LCP[b]	(R)-$(+)$ camphor RCP[b]	(S)-$(-)$ camphor LCP[b]	(S)-$(-)$ camphor RCP[b]	PECD$_{(+)}$[b]	PECD$_{(+)u}$[b]	PECD$_{(-)}$[b]	PECD$_{(-)u}$[b]	ΔPECD[c]	ΔPECD$_u$[c]
c_0^d	1.028	0.972	1.022	0.978	0.056	0.000	0.044	0.000	0.004	0.000
c_1^d	0.048	−0.003	−0.069	−0.014	0.051	0.051	−0.055	−0.055	0.053	0.053
c_2^d	−0.716	−0.639	−0.729	−0.670	−0.077	0.000	−0.059	0.000	−0.006	0.000
c_3^d	−0.070	0.037	0.091	−0.019	−0.106	−0.106	0.110	0.110	−0.108	−0.108
c_4^d	0.014	0.010	0.016	0.017	0.003	0.000	−0.001	0.000	0.002	0.000
c_5^d	0.014	−0.002	−0.007	0.007	0.015	0.016	−0.014	−0.014	0.015	0.015
c_6^d	−0.001	0.000	−0.007	−0.002	−0.002	0.000	−0.005	0.000	0.002	0.000
c_7^d	0.006	0.007	−0.003	0.001	−0.002	−0.002	−0.003	−0.004	0.001	0.001
c_8^d	−0.004	−0.003	0.006	0.003	−0.001	0.000	0.002	0.000	−0.002	0.000

Table 1. Legendre coefficients from camphor determined directly from data presented in Figure 4 and 5.

Coefficients extracted from data presented in Figure 4 and 5 using the pBasex algorithm for each data set separately. [a] See Equation (1). [b] The retrieved values are weighted with r^2 (see text) and averaged over the FWHM of the energy distribution. The values are normalized by the mean $\bar{c}_{k0}$ from ionization with LCP and RCP light of the $(+)$- resp. $(-)$-enantiomer (see text). [c] Same as b but normalized by the mean of the $\bar{c}_{k0}$ values from the $(+)$- and the $(-)$-enantiomer (see text). Values additionally multiplied by 0.5. All values are rounded to three decimal places. A direct calculation of the PECD$_{(en)}$ and ΔPECD coefficients from the LCP and RCP coefficients is presented in the Supporting Information Table SI2. Different notations used in deriving the Legendre coefficients are also summarized in the Supporting Information SI3.

and calculate the PECD for each enantiomer and ΔPECD values directly from averaging the LCP and RCP coefficients according to Equation (25):

$$c_{\text{even,en}}^{\text{LCP}} = \frac{1}{2}\left(c_{\text{even,en}}^{d,\text{LCP}} + c_{\text{even,en}}^{d,\text{RCP}}\right)$$

$$c_{\text{odd,en}}^{\text{LCP}} = \frac{1}{2}\left(c_{\text{odd,en}}^{d,\text{LCP}} + c_{\text{odd,en}}^{d,\text{RCP}}\right)$$

(25)

where the minus sign accounts for the change of sign of the odd Legendre coefficients. Table 2 shows these values together with the derived values for the PECD and ΔPECD. The PECD coefficients are derived in accordance with Equation (2), to give Equation (26):

$$c_{l,\text{en}}^{\text{PECD}} = c_{l,\text{en}}^{\text{LCP}} - c_{l,\text{en}}^{\text{RCP}}$$

(26)

Due to Equation (25), $c_{\text{even,en}}^{\text{PECD}} \equiv 0$ and $c_{\text{odd,en}}^{\text{PECD}} = 2\left(c_{\text{odd,en}}^{\text{LCP}}\right)$ [compare to Eq. (3)]. The ΔPECD coefficients are calculated according to Equation (4):

$$c_l^{\Delta\text{PECD}} = c_{l,+}^{\text{PECD}} - c_{l,-}^{\text{PECD}}$$

(27)

These ΔPECD values are also multiplied by 0.5 to facilitate comparison. For both enantiomers each odd-order coefficient possesses similar amplitude and changes its sign on exchanging the enantiomer (see PECD values, column 4 in Table 2). Note that within a set of coefficients from one enantiomer a change in sign appears between the different odd orders as described in the context of Equation (17). This behaviour of the significant odd orders is also observed for fenchone and

norcamphor (see Table 4) where the sign changes between the first and third coefficient.

This procedure delivers values for the odd coefficients of the ΔPECD that are similar to the ΔPECD$_u$ obtained directly by applying the pBasex algorithm on the ΔPECD image (see Table 1) or derived using the coefficients of the LCP and RCP PAD images from both enantiomers (see the Supporting Information SI2). This substantiates the overall linearity of the pBasex algorithm for these experimental conditions of nearly circularly polarized ionization. Under such conditions the best way for a quantitative analysis is to concentrate on the antisymmetric part of the PECD images [PECD$_u$(y,z)] or, if available, on the ΔPECD image (displayed in Figure 6 third row right image).

We now turn to the topic of characterizing the PECD effect with a single number. We calculate the LPECD according to Equation (17) and the QPECD according to Equation (22). For this, we use the averaged coefficients (LCP values of R- and S-camphor, Table 2, second and third column) within the FWHM of the main distribution for ionization with LCP light. We denote the different measures as LPECD$_\odot^{A^{-1}}$ and QPECD$_\odot^{A^{-1}}$, where $\odot$ stands for the FWHM and A^{-1} for the Abel inversion. The LPECD$_\odot^{A^{-1}}$ for both enantiomers of camphor is about $\pm 8\%$ and the QPECD$_\odot^{A^{-1}}$ is around 8.5% (see Table 2, right side). To provide a comparison for the LPECD$^{A^{-1}}$ from the obtained Legendre coefficients [Eq. (17)] and the signals in forward/backward direction of the PECD image [Eq. (16)], the LPECD is derived using all sets of Legendre coefficients [100 sets for all radii, see Eq. (24)], denoted as LPECD$_\oplus^{A^{-1}}$ where $\oplus$ stands for the completely inverted distribution. The whole energy range corresponding to the projected image covers a range from

Legendre polynomial[a]	(R)-(+)-camphor LCP[b] averaged	(S)-(−)-camphor LCP[b] averaged	Calculated PECD$_{(+)}$[c]	Calculated PECD$_{(−)}$[c]	Calculated ΔPECD[d]	Quantification[e]	
c_0	1.000	1.000	0	0	0	LPECD$_{\odot(+)}^{A^{-1}}$	8.0%
c_1	0.026	−0.027	0.051	−0.055	0.053	LPECD$_{\oplus(+)}^{A^{-1}}$ [f]	6.5%
c_2	−0.678	−0.699	0	0	0	LPECD$_{\odot(−)}^{A^{-1}}$	−8.4%
c_3	−0.053	0.055	−0.106	0.110	−0.108	LPECD$_{\oplus(−)}^{A^{-1}}$ [f]	−6.8%
c_4	0.012	0.017	0	0	0	Quantification[g]	
c_5	0.008	−0.007	0.015	−0.014	0.015	QPECD$_{\odot(+)}^{A^{-1}}$	8.3%
c_6	−0.001	−0.004	0	0	0	QPECD$_{\oplus(+)}^{A^{-1}}$ [f]	6.6%
c_7	−0.001	−0.002	−0.002	−0.003	0.001	QPECD$_{\odot(−)}^{A^{-1}}$	8.7%
c_8	−0.004	0.004	0	0	0	QPECD$_{\oplus(−)}^{A^{-1}}$ [f]	7.0%

**Table 2.** Averaged Legendre coefficients from Table 1 and calculated PECD coefficients.

[a] See Equation (1). [b] Values taken from Table 1. For each enantiomer the corresponding Legendre coefficients are averaged, see Equation (25) ($c_{\text{even,en}}^{\text{LCP}} = \frac{1}{2}\left(c_{\text{even,en}}^{d,\text{LCP}} + c_{\text{even,en}}^{d,\text{RCP}}\right)$ and $c_{\text{odd,en}}^{\text{LCP}} = \frac{1}{2}\left(c_{\text{odd,en}}^{d,\text{LCP}} + c_{\text{odd,en}}^{d,\text{RCP}}\right)$). Note that the corresponding RCP values only differ in the sign of the odd coefficients. [c] PECD - in accordance to Equation (2)—derived directly from the averaged coefficients for ionization with LCP light, see Equation (26) ($c_{l,\text{en}}^{\text{PECD}} = c_{l,\text{en}}^{\text{LCP}} - c_{l,\text{en}}^{\text{RCP}}$). [d] Difference of the obtained PECD values, see Equation (27) ($c_l^{\Delta\text{PECD}} = c_{l,+}^{\text{PECD}} - c_{l,-}^{\text{PECD}}$), multiplied by 0.5. [e] LPECD according to Equation (17), using the averaged coefficients ($\odot$ stands for the FWHM and A^{-1} for Abel-inverted data) for ionization with LCP light. [f] Quantification for all c_{kl} sets in a range from approx. 0–1.1 eV (equivalent to the measured PAD image), indicated by $\oplus$. [g] QPECD derived by Equation (22), using the averaged coefficients for ionization with LCP light. Note that the ΔPECD coefficients from the averaged coefficients are similar to the coefficients obtained directly from the pBasex and are listed in Table 1. After deriving the quantitative measures the calculated coefficients are rounded to three decimal places.

approx. 0–1.1 eV. We get a $LPECD_{\oplus}^{A^{-1}}$ of about $\pm 7\%$ and a $QPECD_{\oplus}^{A^{-1}}$ of around 7% (see Table 2, right side). Table 3 lists the quantitative values that are retrieved from the PECD images ($LPECD_{\oplus}^{A}$, where A stands for the Abel-projected data resp. images). The $LPECD_{\oplus}^{A^{-1}}$ values derived for the whole set of Legendre coefficients are similar to the ones that are directly obtained from the PECD images ($LPECD_{\oplus}^{A}$), illustrating the equivalence of Equations (16) and (17). The PPECD values ($PPECD_{\oplus}^{A}$) are derived using Equation (23) comprising the absolute squared signals of the antisymmetric part of the PECD images ($PECD_u(y,z)$)^2. The $PPECD_{\oplus}^{A}$ values for camphor are about 8%. Deviations in the PECD for both enantiomers of camphor and the obtained quantitative values may be related to different enantiomeric purities (see next subsection). In summary, we observe that there is a difference when comparing quantifications taking only electrons at the FWHM of the

excess energy into account to quantifications taking all measured electrons over the whole energy range into account. In the case under study, values obtained from excess energy data are higher in comparison to values from all data hinting to additional processes at play. This topic is discussed further in Section 3.1.3.

3.1.1. Ellipticity Dependence

We now investigate the qualitative and quantitative sensitivity of the PECD effect with respect to the polarization state. To that end we measure the dependence of the PECD on the ellipticity of the ionizing photons. Applying a quantitative analysis on the results using the PPECD values, we will be able to quantify the relation between the circularity of the polarization state and the PECD effect. The results are shown in Figure 7:
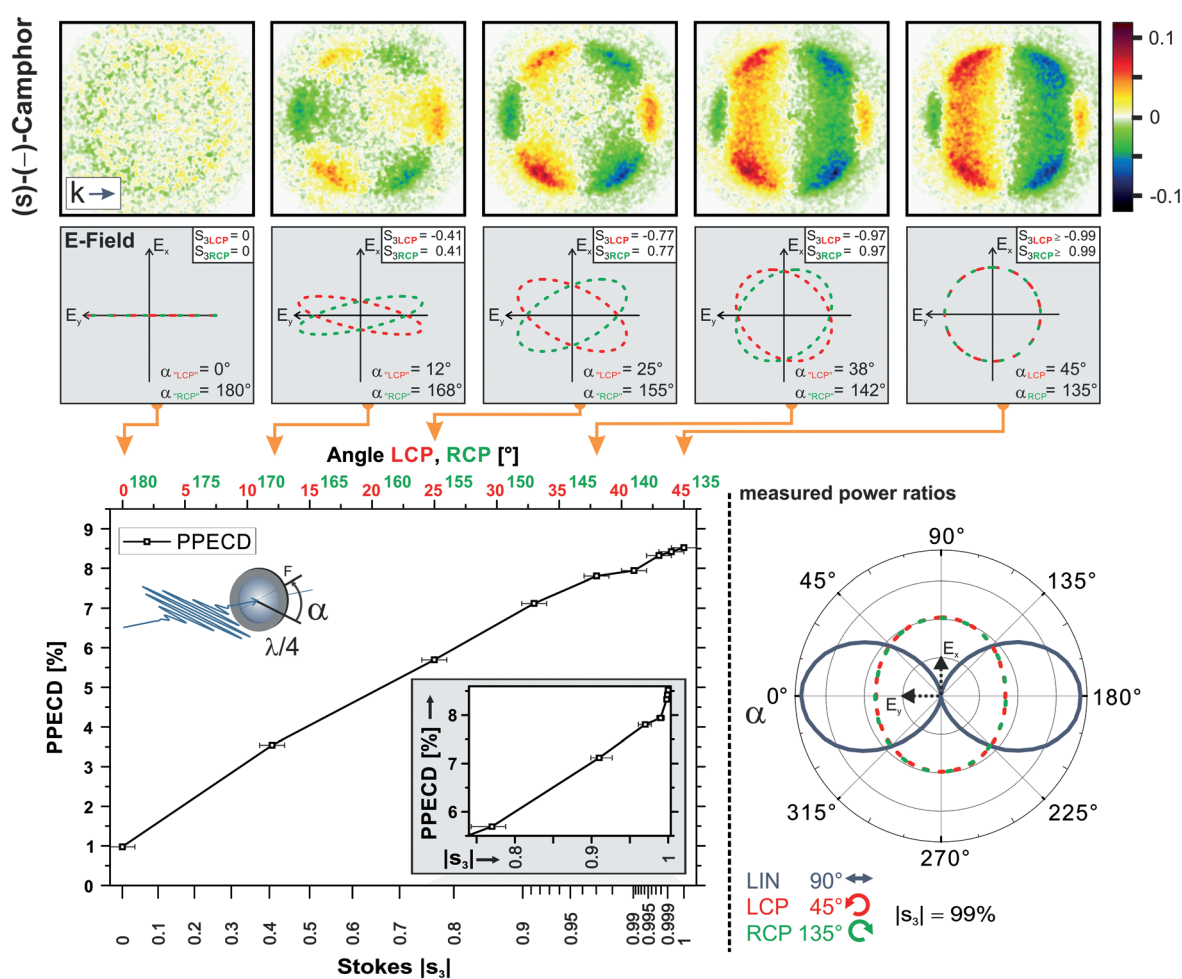
Figure 7. Ellipticity dependence of the PECD of (S)-(−)-camphor: Top row: Antisymmetric part of the PECD images measured at different polarization states with equal ellipticity but different helicity. Left image: (S)-(−)-camphor measured with a pair of linear polarization states showing no distinctive antisymmetry with respect to the laser propagation. The circularity of the used polarization states was successively increased until both polarizations were completely circular (right image). An alternation of the polarization was achieved by changing the angle α_{LCP} and α_{RCP} between the fast axis of the QWP and the polarization axis of the incoming light. Note the increasing amplitude of the antisymmetric PECD images with increasing circularity of the ionizing laser pulses. The right image measured at LCP and RCP is in accordance with the PECD on (S)-(−)-camphor displayed in Figure 5 (second row, right). Middle row: Corresponding electric field of the polarization states for each measurement. The derived Stokes S_3 parameter is specified for both polarization states. Bottom row, left image: Evaluation of the measured antisymmetric PECD parts for different polarization states using the PPECD [see Eq. (23)]. Note the overall nonlinear dependence of the PPECD with respect to $|S_3|$ (see inset). The PECD is maintained even for light with low ellipticity. Bottom row, right image: Experimental power ratios measured for LCP and RCP using an additional polarizer. The Stokes S_3 parameter in these cases is determined to be $|S_3| = 99\%$ (further details are given in the Supporting Information SI4).

(S)-($-$)-camphor is measured alternately with laser pulses of polarization states of equal ellipticity but different helicity. PECD images of these measurement pairs are derived and the antisymmetric parts [PECD$_u$(y,z)] are presented in Figure 7 top row. The circularity of the involved polarization states is successively increased until both polarizations are completely circular, matching the data set on camphor presented before (see also Figure 5 and 6). Experimental power ratios are measured for LCP and RCP light using an additional polarizer and are presented in the third row of Figure 7, right image. The semi-axes with respect to the 0° and 90° directions exhibit a power ratio of $\approx$1.25, hence the derived value of the Stokes S_3 parameter[60–62] is $|S_3| = 99\%$ (see Supporting Information SI4). Different polarization states are realized by changing the angle between the fast axis of the QWP and the polarization axis of the incoming light. Starting with a pair of two LIN measurements (see Figure 7, top row left image) no structured antisymmetric components appear in the difference image. In this case, a PPECD value of approx. 1% may be related to inaccuracies in setting the angles of the QWP and also due to accumulation of noise in the antisymmetric part of the PECD image. Further averaging could reduce the latter contribution. Increasing the circularity of the polarization states, leads to an increase of the amplitude in the antisymmetric part of the PECD images. For illustration, the time-dependent electric field vector, derived from the angle of the QWP, is plotted in Figure 7, second row. For a further quantification of the ellipticity dependence, the measured PAD images with the same ellipticity but a different helicity—obtained under similar conditions as described before—are analysed without further normalization. In this case the prerequisites for applying an Abel inversion are not given and for a quantitative evaluation the PPECD measure [see Eq. (23)] is applied on the antisymmetric part of the PECD images. Resulting PPECD$_\oplus^A$ values for each pair of measured elliptical polarization states are plotted in Figure 7, third row, left image. The errors on the abscissa are due to the alignment of the QWP and are estimated to be below 1 degree. Ambiguities in the determination of the centre of the image are estimated to be below 5 pixel with respect to the CCD resolution. They would be represented by an error on the ordinate. In our case, this error is smaller than the presented symbols for the data points. The measured PPECD as a function of the ellipticity shows a monotonic increase. In addition, we note that even for light with a rather weak elliptical polarization, that is, a small angle of the fast axis with respect to the ingoing laser polarization, a significant PECD effect is observed. Furthermore, a nonlinear dependence of the PPECD with respect to $|S_3|$ as indicated in the inset in Figure 7, third row, left image, is observed.
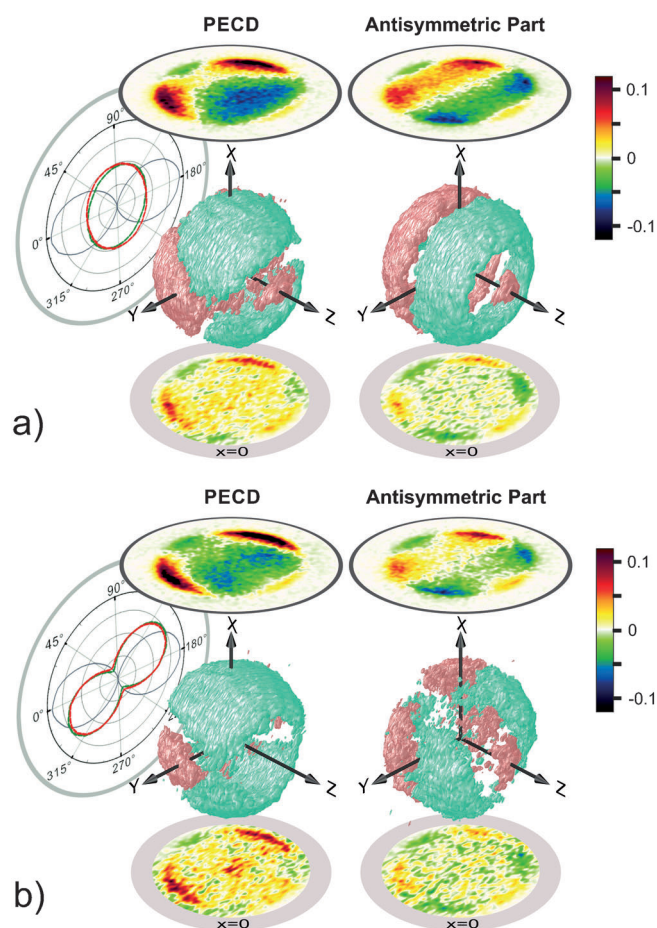
3.1.2. 3D-PECD via Tomographic Reconstruction

In this section we focus on an alternative approach to evaluate the PECD effect for elliptical polarization states as well. As mentioned above, a lack of cylindrical symmetry precludes the inversion via reconstruction methods such as, for instance, the pBasex algorithm. Instead, we use our tomographic reconstruc-

tion method[31,33,34] to measure a symmetry-independent three-dimensional PECD effect (3D-PECD). First, in order to reproduce the PECD images [PECD(y,z)] for cylindrical symmetric distributions, we measure the tomographic reconstruction for ionization with LCP and RCP light. We use S-camphor to reproduce the Abel-inverted PECD image as presented in Figure 6, second row. Secondly, we will demonstrate a case of ionization with elliptically polarized light.

To perform our tomographic reconstruction method, an achromatic half-wave plate (HWP) is introduced in the optical setup behind the QWP and rotated by about 90° in steps of 1°. The HWP is used to rotate the polarization state of the incoming light from 0° to 180° as described for example in Ref. [34]. Note that a HWP turns the helicity of light, that is, changes the sign of the Stokes S_3 parameter. It also changes the Stokes S_2 parameter, representing the amount of linearly $\pm45°$ polarization, in sign. The power ratios from the applied polarization states, displayed in Figures 8 a,b on the right side, are measured using an additional polarizer and adjusting the fast axis of the HWP at zero degree. LCP (red) and RCP (green) possess power ratios similar to Figure 7, third row, right plot, with a derived Stokes S_3 parameter of $|S_3| = 99\%$ (further details are given in the Supporting Information SI4). A polarization measurement of the LIN light, entering the HWP, is sketched in grey.

A series of PAD images from 90 projections (see above) is used to reconstruct this 3D-distribution via a Fourier-based tomographic reconstruction algorithm.[69] Pairs of PAD images for each position of the HWP are recorded subsequently for the two desired polarizations from the QWP, in this case LCP and RCP light. In total, every angle of the HWP for LCP or RCP light includes approximately 30 000 laser pulses. Therefore, a measurement of a reconstructed 3D-PAD for each polarization corresponds to about an order of magnitude increase of data as compared to the results presented in Section 3.1.

To obtain a 3D-PECD, we subtract the three-dimensional reconstructed distributions for RCP from the LCP distribution. The result is shown in Figure 8 a. The colour coding of the iso-surfaces is chosen to be pink for positive and turquoise for negative values. For visualization purposes, threshold values for these iso-surfaces have been chosen for each reconstruction to include only signals slightly higher than the signal height at the FWHM in the main distribution. An asymmetry with respect to the laser propagation direction is clearly visible in the 3D-PECD data. We also obtain the projection of the 3D-PECD and its antisymmetric part via numeric integration from the retrieved 3D-PECD distribution along the x-axis. Those are displayed on top and can be directly compared to Figure 5, second row, left and right image. As expected, the projections from the tomographic data and the directly measured projections match very well. The antisymmetric part of the 3D-PECD (shown in Figure 8 a, right panel) is derived via a three-dimensional 180° back-folding along the z-axis with respect to the xy-plane. It reveals the contribution of the first and third Legendre polynomials that are cylindrically symmetric in shape with respect to the z-axis and antisymmetric in signal with respect to the xy-plane. The 3D-PECD data allows the analysis of

Figure 8. a) Three-dimensional PECD (3D-PECD) from subtraction of tomographically reconstructed PADs from (S)-(−)-camphor originating from ionization with LCP and RCP laser pulses. Experimental power ratios measured for LCP (red) and RCP (green), using an additional polarizer, are displayed on the left side. For clarity, a polarization measurement of the LIN light, entering the HWP, is sketched in grey. The measured projected PECD image and its antisymmetric part (according to Figure 5, second row, left and right image) are displayed on top. Resulting from the tomographic reconstruction, the obtained 3D-PECD is displayed using iso-surfaces. The pink areas represent positive and the turquoise areas represent negative signals. For visualization, threshold values for these iso-surfaces have been chosen to include only signals higher than the signal height of the FWHM in the main distribution. Slices in the (y,z)-plane from the 3D-PECD are shown on the bottom. Reconstruction artefacts outside of the main distribution have been removed. These slices are similar to the Abel-inverted images from the pBasex algorithm (see Figure 6, second row left and right image). The antisymmetric part of the 3D-PECD is derived via a three-dimensional 180° back-folding along the z-axis with respect to the (x,y)-plane. It reveals the contribution of the first and third Legendre polynomials that are cylindrically symmetric in shape and antisymmetric in signal with respect to the z-axis. Note the good agreement of data reconstruction with the pBasex algorithm in these antisymmetric data using circular polarization. b) 3D-PECD as described above, but from ionization with elliptically polarized laser pulses. Concerning the amplitude of the Stokes $|S_3|$ parameter (see Supporting Information SI4), the presented measurement is in some way equivalent to Figure 7, top row, third PECD image but with elliptical polarizations having parallel main axes. Note that the asymmetry contribution coincides with the main axis of the elliptical polarization.

any slice through the distribution. Comparing for instance the (y,z)-slice at $x=0$ obtained from the tomographic reconstruc-

tion (Figure 8a, bottom) to the corresponding Abel-inverted PECD images (see Figure 6, second row left and right image) shows convincing agreement.

Because the photoelectron distributions resulting from circularly polarized light entails a cylindrical symmetry about the k-vector, the $x=0$ and $y=0$ slices through the 3D-PECD are equivalent. As a check, we extract the Legendre coefficients for the $x=0$ and $y=0$ slices. In these cases, the axis of cylindrical symmetry for the Legendre polynomials is parallel to the k-vector. The averaged values of the Legendre coefficients agree well with the presented values for S-camphor (see Table 2). For example, the coefficients of the first and third Legendre polynomial deviate less than 5% from the S-camphor LCP values resulting from the Abel-inverted data. Within the FWHM of the tomographically reconstructed main distribution the $LPECD_{\odot(−)}$ is about −8.3% and the $QPECD_{\odot(−)}$ is about 8.9%. Corresponding values from Table 2 are −8.4% and 8.7%. This example demonstrates that the three-dimensional tomographic reconstruction approach includes data analysis based on Abel inversion. However, the analysis based on tomographic reconstruction can be generalized to non-cylindrically symmetric objects.

In order to investigate the 3D-PECD for a case without cylindrical symmetry, we adjust the QWP to generate elliptically polarized light of different helicity for the ionization of S-camphor. The tomographic measurement was similarly performed and evaluated as described above. The results are shown in Figure 8b. Note that ionization with LIN light creates most of the photoelectron signal within the polarization axis (see Figure 4). To minimize symmetrical components in the three-dimensional PECD distribution, which could arise due to the large linear components, we set the main axis of both elliptical polarizations to be parallel. Thus, for this elliptical PECD measurement, the angles between the fast axis of the QWP and the polarization axis of the incoming light are set to be 115° for left-handed elliptically polarized light (LELLIP) and 25° for right-handed elliptically polarized light (RELLIP). The measured power ratios for LELLIP (red) and RELLIP (green) are displayed in Figure 8b) left side. Concerning the circularity, that is, the S_3 parameter, the presented measurement is approximately equivalent to Figure 7, top row, third PECD image (see Supporting Information SI4). There is only a difference in the diagonal component of the linear fraction in the polarization state, that is, the sign of the S_2 parameter, comparing the elliptical polarization at 115° and 155°.

As expected from the ellipticity scan (Figure 7) the asymmetries in the 3D-PECD with respect to the laser propagation direction are not as distinctive as in the case of ionization using circularly polarized laser pulses but are still clearly visible. The reconstructed antisymmetric signals are no longer cylindrically symmetric to the z-axis and coincide with the main axis of the elliptical polarization. This might be a hint to field-induced polarisabilities of the intermediate state being different for the two perpendicular axis of the elliptical polarization. Note that field induced polarisability of the intermediate was used to simulate higher-order polynomials in the PECD after one-photon ionization of camphor out of a resonant intermediate.[37] Higher-order polynomials direct from ground-state mul-

tiphoton ionization have been calculated making use of a continuum-state corrected strong-field approximation.[68]

Note that the wealth of information obtained in these projected images under many different angles might also be a route for a complete determination of the photoionization dynamics of chiral molecules. Although this might be a challenging task, initial steps to a complete photo-ionization experiment based on this approach have been demonstrated recently.[35]

3.1.3. Intensity Dependence of the PECD

In order to analyse the excitation and ionization mechanism in more detail, we study the PAD images and the TOF-MS as a function of the laser intensity. First, we determine the multi-photon power laws. Then we turn to a discussion of intensity-dependent fragment distributions and finally investigate ponderomotive shifts in the PADs. All observations hint to a 2+1 REMPI process on the parent molecules as the dominant origin of the observed PECD effect, where non-resonant contributions from the parent ground state or contributions from fragments are small.

We measured the PAD images as well as TOF-MS under identical conditions in an intensity range from 0.5–2.8 I_0. From the ionization potential we expect a three-photon ionization out of the highest occupied orbital and from the absorption spectrum we expect a 2+1 REMPI process (see below and Figure 11). To confirm three-photon ionization, we measured the total photoelectron signal [T in Eq. (10)] as a function of the laser intensity. The power law of the ionization process is extracted from a double logarithmic plot of T versus the laser intensity. These power laws are determined for the Abel-inverted PAD images as well as for the TOF-MS data in the intensity range from 0.5–2.1 I_0. To this end, Abel-inverted PAD images without normalization were investigated for the contributing total signal c_0 in different ranges of energy. In the FWHM energy range of the main distribution the power laws show a multiphoton exponent of about 2.9 at low intensities and of about 2.6 at high intensities with a standard deviation of approximately 0.3. These power laws support the 2+1 excitation scheme but also indicate an onset of saturation effects. Note that the presented multiphoton exponents of the PAD images are close to the results in our previous publication[22] when approaching higher intensities. The photoelectrons with a very low kinetic energy, being smaller than 0.02 eV, did not originate from residual gas. They possessed as well as the photoelectrons from 0.02–0.40 eV a slightly larger exponent in comparison to the main distribution in the PAD image and did not show a PECD effect (see below). These results indicate the presence of other ionization processes. Thus, quantitative determination methods considering the whole projected distribution can deliver different values. This explains why the LPECD and QPECD values on the excess energy are higher than the values derived from the whole distribution (see Table 2). The obtained exponents for the parent-ion yields are between 2.7 for low intensities and 2.5 for high intensities also with a standard deviation of approximately 0.3. These parent-ion yields

show slightly smaller values due to increasing fragmentation and match the results for the main distribution in the Abel-inverted PAD images (see above).

We turn back to a qualitative comparison of the mass spectra to the corresponding PECD images at the applied intensities. The measured TOF-MS from camphor are dominated by the parent ion. A typical TOF-MS for ionization of (S)-(−)-camphor using LCP light at I_0 is given in Figure 2 and Figure 9 (second row). The fragments at lower masses in the TOF-MS show power law exponents that are roughly greater by one. This indicates the absorption of another photon as compared to the parent-ion yields. These appearing fragments can be assigned assuming simple bond breaks. The occurring fragments match with known mass spectra from electron-impact ionization.[65,70] With decreasing intensity, an increase of the relative parent-ion yield in comparison to the fragments at lower masses was observed (see Figure 9, second row). However, the PECD on the excess energy of camphor does not significantly change its shape by variation of the intensity (see Figure 9, first row). A significant change in the dominant ionization processes for the PECD effect is therefore not observed in this intensity interval. The quantitative analysis shows a small decrease of the absolute values with respect to higher peak intensities (see the Supporting Information Figure SI1). From this observation, we deduced dissociative ionization as the dominant underlying process for the PECD,[22] that is, ionization precedes fragmentation.[71] This dissociative ionization was recently confirmed by coincidence techniques.[36,37]

We now turn to the discussion, whether ionization from the ground state or from an intermediate resonance is the origin for the observed PECD effect. We concentrate again on the PAD images from camphor measured at increasing intensities. The photoelectron distribution in the PAD images reveals only very minor shifts in the excess energy to lower energies (see Figure 9) that are independent with respect to LIN or LCP and RCP ionization. In contrast, for the ionization of Xenon with LIN light ponderomotive shifts[58] of about 100 meV to lower energies of the measured photoelectron excess energies are observed in this intensity range (see Figure 10). This result indicates that the photoelectron distribution originates from the intermediate states acting as Freeman resonances.[72–76] To higher intensities further distributions of photoelectrons with energies below the FWHM of the main distribution are observed in the PAD images but do not show a significant PECD effect (see Figure 9 upper row). Due to the absence of a PECD effect these additional electron contributions are attributed to other ionization processes such as fragment ionization. Note that no significant change in the shape of the PECD was observed with respect to pressure variations[22] in a range of 1–6×10^{-6} mbar ruling out space charge effects.

In addition, we also observe a pronounced PECD in the first above-threshold-ionization (ATI) signal that is modulated with yet higher-order Legendre polynomials. A detailed analysis of the ATI-PECD on camphor, fenchone and norcamphor will be discussed in a forthcoming publication.[77]
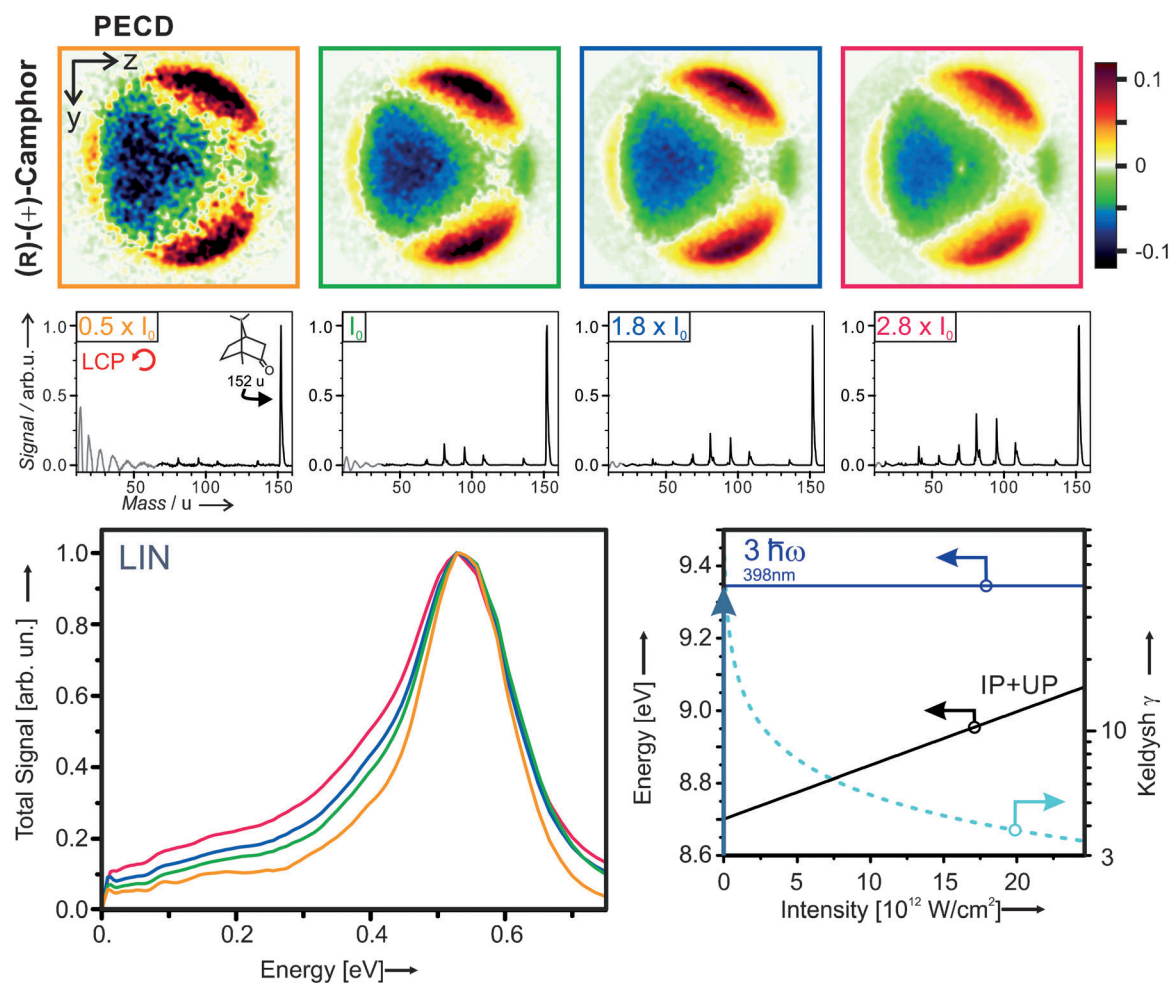
Figure 9. Intensity dependence of camphor. Top row: PECD images from *R*-camphor at various peak intensities out of a series of eight consecutive measurements in a range of ≈ 0.5–$2.8\,I_0$. Note that the observed PECD images do not show significant changes in the angular and energy distribution. Corresponding mass spectra at the same conditions as the displayed PECD images are shown in the middle row. The mass spectra from ionization with LCP light are normalized to the signal of the parent ion. The oscillations, which are greyed out, are electronic noise at low signal levels. Bottom row, left: Total photoelectron signal as a function of energy derived from the corresponding $100\,c_0$ coefficients obtained from Abel inversion and making use of Equation (10) from *R*-camphor ionized with linearly polarized laser pulses at various peak intensities, normalized to the maximum of the energy distribution. Note that the photoelectron signal from the ionization with circularly polarized light shows the same intensity dependent behaviour. Bottom row, right: Calculated ponderomotively shifted vertical ionization potential of camphor, that is, 8.7 eV,[85] for different peak intensities. The horizontal line indicates the energy of three 398 nm photons in the multiphoton ionization. The blue dashed line is the derived Keldysh γ parameter for camphor, reaching a value larger than three at highest peak intensity, thus indicating a multiphoton regime.

3.1.4. Comparison to Other Results

We proceed by comparing the results of camphor presented in this contribution with our previous results[22] and recently published data from Janssen and coworkers.[37]

Taking the different experimental conditions and the above-mentioned ellipticity and intensity dependence of the PECD into account, our results are consistent with our previous work and the results of Janssen and coworkers. The quantitative PECD values obtained for camphor in this contribution and the previous publications are very similar. Janssen and coworkers specified values of: $\mathrm{LPECD}_{\odot(+)}^{A^{-1}} = 8.5\,\%$ and $\mathrm{LPECD}_{\odot(-)}^{A^{-1}} = -7.3\,\%$ where our terminology is used for quantification on the photoelectron excess energy range. They used a peak intensity of 1–$2\times10^{12}\,\mathrm{W\,cm^{-2}}$ and a longer pulse duration. In this contribution at about $4\times10^{12}\,\mathrm{W\,cm^{-2}}$ peak intensity, a $\mathrm{LPECD}_{\odot(+)}^{A^{-1}} =$

$8.0\,\%$ and $\mathrm{LPECD}_{\odot(-)}^{A^{-1}} = -8.4\,\%$ (see Table 2) is determined. In our previous publication at about $5\times10^{13}\,\mathrm{W\,cm^{-2}}$, the following values correspond to the presented coefficients there: $\mathrm{LPECD}_{\odot(+)}^{A^{-1}} = 6.9\,\%$, and $\mathrm{LPECD}_{\odot(-)}^{A^{-1}} = -7.2\,\%$. The slight decrease with increasing intensity is consistent with our intensity analysis given above and in the Supporting Information SI1.

Secondly, the first and third Legendre coefficients in the PECD and ΔPECD here (Table 1) match our results reported in Ref. [22] and those of Janssen and coworkers very well. The ratios between the first and third Legendre coefficients are also quite similar and remain nearly constant as a function of intensity (see Supporting Information Figure SI1).

With respect to the ellipticity dependence of the PECD, which showed an overall nonlinear dependence with respect to $|S_3|$ (see Section 3.1.1), small discrepancies with respect to
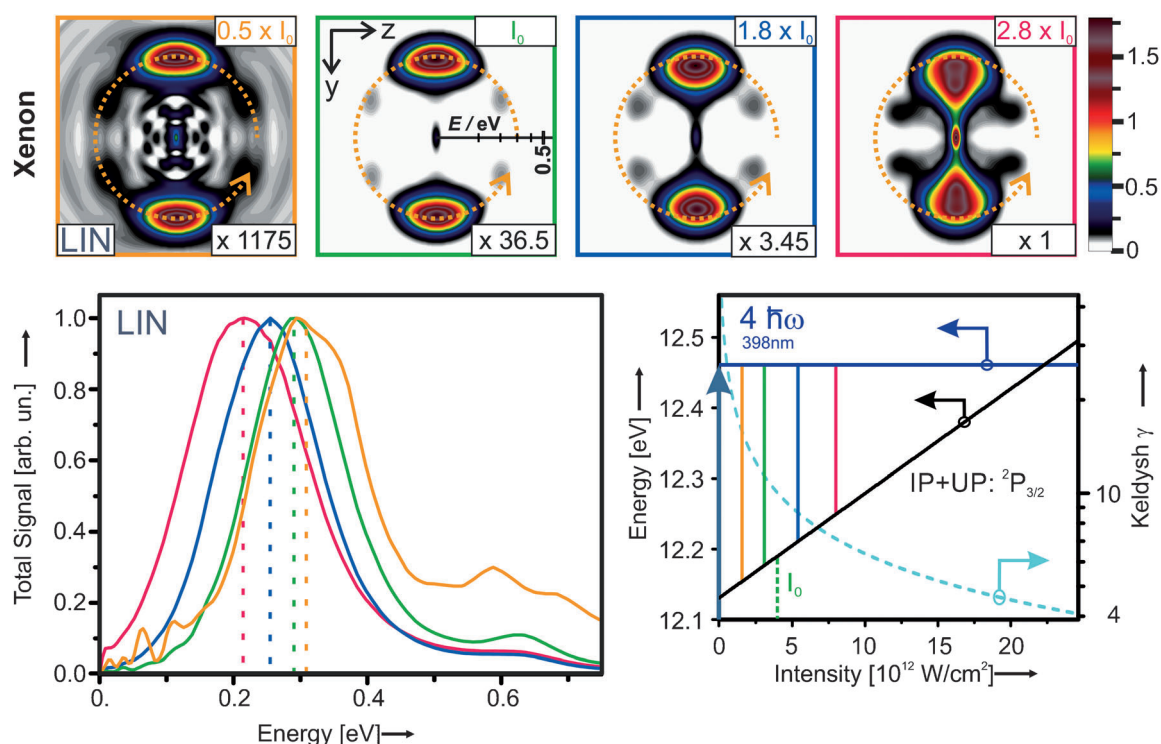
Figure 10. Ponderomotively shifted electron signal from ionization of Xenon at 398 nm. Upper row: Four Abel-inverted PAD images from Xenon, ionized with LIN laser pulses out of a series of eight consecutive measurements under similar conditions as in Figure 9. For comparison, a particular scaling factor indicated in the inset is used for the colour scale. The peak intensity in the displayed measurements is increased from left to right ranging from ≈ 0.5 to $2.8\ I_0$. All PAD images have been recorded in the same energy range and an energy scale is exemplarily depicted in the second image. In order to visualize the observed ponderomotive shift, which appears in the same way ionizing with circularly polarized light, an orange dashed ring at ≈ 300 meV indicates the maximum of the photoelectron energy distribution from xenon at the lowest intensity, namely $\approx 0.5\ I_0$ and is displayed in the four images. Lower row, left: total photoelectron signal as a function of energy derived from the corresponding 100 c_0 coefficients obtained from Abel inversion and making use of Equation (10) at various peak intensities, normalized to the maximum of the energy distribution. Lower row, right: Calculated ponderomotively shifted ionization potential from the Xe II $^2P_{3/2}$ ionic state for different peak intensities. The horizontal line indicates the energy of four 398 nm photons in the multiphoton ionization and the vertical lines represent the measured excess energies peaking in the photoelectron distributions. The blue dashed line is the derived Keldysh γ parameter for Xenon, reaching a value of approximately four at highest peak intensity, thus indicating a multiphoton regime.

the determined quantitative values of Janssen and coworkers[37] might be correlated with the differing Stokes S_3 parameters for their LCP and RCP light in comparison to our S_3 parameters. From a data acquisition and analysis point of view, Janssen and coworkers applied the coincidence technique[78,79] and measured the central section of the PAD. This time sliced electron image is a projection of photoelectrons with an ejection angle of $\pm 25°$ with respect to the centre of the image and the plane parallel to the detector surface. The resulting distribution comprises about 46 % of all emitted electrons[80] and is fitted with the Legendre polynomials. In our VMI set-up, the PAD is projected onto the detector and inverted using the pBasex algorithm. These differences regarding the measurement technique, the enantiomeric purities of the used specimen and the laser properties such as the central wavelength, the applied peak intensity and the amount of circularity of the polarization states make a direct quantitative comparison on the absolute values of the LPECD with the results from Janssen and coworkers difficult. However, the similar results in the ratios of the retrieved odd coefficients as well as the range of the absolute quantification values indicate robustness against experimental parameters.

In the initial measurements on camphor and fenchone reported in Ref. [22] some inhomogeneities on the MCP detector have been found. The additive inhomogeneities affected the measured PAD images but did not influence the PECD images significantly. The PECD data presented here are measured with a new MCP detector. Regarding the even polynomials, the second-order polynomial now delivers, apart from the zeroth order, the highest values and is much stronger than the fourth polynomial. This qualitative observation is consistent with the results from Janssen and coworkers. Remaining discrepancies regarding the quantitative values and ratios of the even polynomials may be related to the different detection or reconstruction method, as described above.

3.2. PECD on the Bicyclic Ketones

In order to evaluate the utility of the PECD for molecular identification and to infer systematic trends in the PECD, we investigate the PECD of different chiral bicyclic ketones. In addition to the studies on camphor, we measured the PECD of fenchone and norcamphor. The abovementioned quantification facilitates a comparison of these chiral molecules both in the

contributing Legendre coefficients and the total effect. All of the investigated bicyclic ketones exhibit a PECD effect in the range of up to ±15%, each with a different set of amplitudes and signs of the odd Legendre polynomials.

The enantiomers of camphor and fenchone as well as the racemic norcamphor were purchased from Sigma–Aldrich and (S)-(+)-norcamphor from Chemische Laboratorien Dr. Soenke Petersen. Our chiral substances possess a constitutional purity of over 98% and in particular: (R)-(+)-camphor 98.43%, (S)-(−)-camphor 99.6%, (S)-(+)-fenchone 99.2%, (R)-(−)-fenchone 99.2%, (S)-(+)-norcamphor > 98% and (RAC.)-(+/−)-norcamphor > 98%. The enantiomeric purities, termed enantiomeric excess (ee), for (R)-(+)-camphor and (S)-(−)-camphor are deduced from the optical rotatory power given in the certificates of analysis from Sigma–Aldrich to be > 98%. Furthermore, for the fenchone specimen gas chromatography was performed by Chemische Laboratorien Dr. Soenke Petersen using a γ-cyclodextrin capillary column.[81,82] This analysis revealed an ee of 99.8% for (S)-(+)-fenchone and 84.0% for (R)-(−)-fenchone with a measuring error in the range of ±0.1% ee. These values are in agreement with the expected enantiomerical purity deduced from the optical rotatory power given in the certificates of analysis from Sigma–Aldrich. For (S)-(+)-norcamphor an enantiomeric excess of over 95% is specified by Chemische Laboratorien Dr. Soenke Petersen.

These molecules are quite similar in mass or structure. Fenchone and camphor have the same mass and the same constituents but feature a different arrangement of the substituents. Norcamphor is a derivative of camphor in which the methyl substituents are replaced by hydrogen, resulting in a smaller mass.

Figure 11 shows the ionization schemes for the studied bicyclic ketones at room temperature adapted from Pulm et al.[83] As discussed above, ionization proceeds via a 2+1 REMPI process. The B-band, occurring on all the three bicyclic ketones, acts as the resonant intermediate state. In contrast to camphor and fenchone, clear vibronic structures can be seen in the B-band of the absorption spectrum of norcamphor. High-resolution spectra from the 2+1 ionization of molecules in a cold beam in a range from 384–418 nm reveal numerous narrow resonances[84] that have been recently reproduced and extended for camphor by Janssen and coworkers.[37] The vertical ionization potentials (IPs) of the three ketones are around 9 eV, that is, 8.7 eV for camphor,[19,85,86] 8.6 eV for fenchone[16] and 9.17 eV[87] for norcamphor. Since the energy of the three photons required for ionization is about 9.35 eV, ionization can only occur from the highest occupied orbital.[16,85]

We confirmed the three-photon ionization as detailed for camphor (see Section 3.1.) by measuring the power laws for fenchone and norcamphor as well. The resulting multiphoton exponents are similar to those derived for camphor. For the chosen intensities, measured TOF-MS are dominated by the parent ion for each of the investigated bicyclic ketones. An increase of the relative parent-ion yield in comparison to the fragments at lower masses is also observed for fenchone and norcamphor with decreasing intensity. This again hints to an underlying dissociative ionization process. No significant
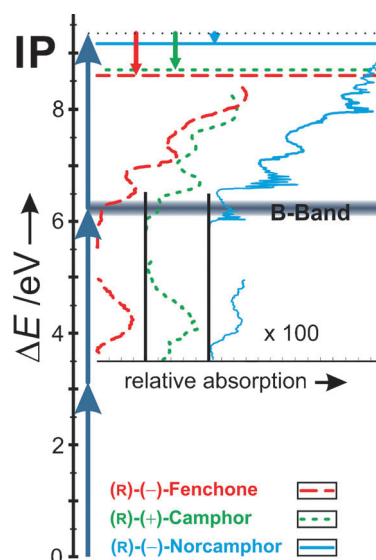

Figure 11. Excitation and ionization scheme of the bicyclic ketones fenchone (red), camphor (green) and norcamphor (blue) adapted from Pulm et al.[83] The vertical IPs are: camphor: IP: 8.7 eV,[85] fenchone: IP: 8.6 eV,[16] norcamphor: IP: 9.2 eV.[87] The expected excess energies from the threshold ionization are indicated by the coloured arrows, for example, in the case of norcamphor a higher IP leads to lower kinetic energies in comparison to camphor and fenchone.

change is observed on the excess energy of the main photoelectron distribution and of the shape of the PECD images as a function of intensity. This indication of involved Freeman resonances underscores again the 2+1 REMPI process being at play.

The PECD results of our measurements on the bicyclic ketones are presented in Figure 12. The ungerade parts of the measured PECD images together with the corresponding Abel-inverted images of the three bicyclic ketones are displayed. Obtained excess energies peak at the following values: camphor at 0.52 eV, fenchone at 0.56 eV and norcamphor at 0.23 eV, all with a FWHM of approximately 200 meV. The resulting excess energies for camphor and fenchone are in agreement with our previous measurements[22] but about 200 meV lower than expected from the abovementioned vertical ionization potentials from synchrotron experiments. For camphor the value of the excess energy was reproduced by Janssen and coworkers.[36,37] For norcamphor the measured excess energy agrees with our total photon energy of about 9.35 eV and the vertical IPs reported on He I photoelectron spectra,[86–89] ranging from 8.94–9.17 eV. The deviation of the excess energy as expected from the vertical IP hints to a dynamical[90] or static[37] resonance behaviour.

Besides the differences in the excess energy of the investigated ketones, there are pronounced differences in the PECD despite the similarity of their chemical structure. This may be an additional hint to the importance of the scattering state for this relatively low-kinetic-energy electrons released in the multiphoton process.[68,91,92] For quantification, the same procedure as detailed for camphor has been applied and the results are summarized in Table 3 (LPECD and PPECD derived from Abel-transformed distributions) and Table 4 (Legendre coefficients,
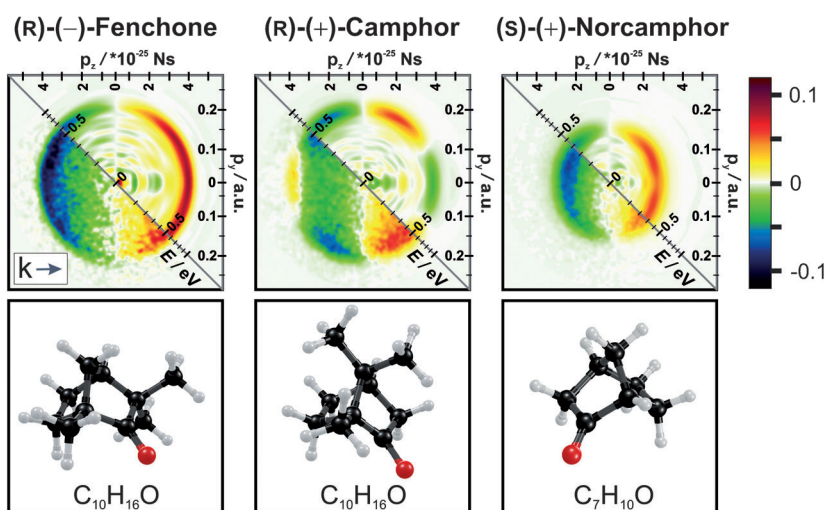
Figure 12. Upper row: Antisymmetric part of the PECD images from the bicyclic ketones fenchone, camphor and norcamphor. The images above the diagonal show the Abel-inverted image with calibrated scales of energy and momentum. The maxima in the PECD images and the Abel-inverted images are observed at ≈ 0.56 eV for fenchone, ≈ 0.52 eV for camphor and at ≈ 0.23 eV for norcamphor. Lower row: Corresponding three-dimensional structure together with the molecular formula.

efficients are mainly contributing. The noted change in sign for the first- and third-order coefficients for camphor is also observed for fenchone and norcamphor. The difference in the derived values of both enantiomers of fenchone $LPECD^{A^{-1}}_{\odot(+)} = -13.8\%$ and $LPECD^{A^{-1}}_{\odot(-)} = 10.9\%$ correlate with the different values for the enantiomeric excess (see above). This result motivated an extended enantiomeric excess sensitivity study which is currently under way in our labs.[93]

As a first test for the utility of PECD as an analytical tool, we compare the extreme cases: the enantiomerically pure specimen and the racemic species by using the quantitative evaluation of the PECD images taking norcamphor as an example.

For (S)-(+)-norcamphor and (RAC)-(+/−)-norcamphor the antisymmetric part of the PECD images are shown in

LPECD, QPECD derived from Abel-inverted data). In contrast to camphor, where the third Legendre polynomial is dominating the PECD, for fenchone and norcamphor the first Legendre co-

Table 3. Quantification on the bicyclic ketones (projected data).

|	(R)-(+)-camphor	(S)-(−)-camphor	(R)-(−)-fenchone	(S)-(+)-fenchone	(S)-(+)-norcamphor	(RAC.)-(+/−)-norcamphor
$LPECD^{A}_{\oplus}$ [a]	6.5%	−6.8%	9.1%	−10.1%	6.8%	0.0%
$PPECD^{A}_{\oplus}$ [b]	7.9%	8.4%	11.0%	12.4%	7.5%	0.9%

[a] Values obtained from the PECD images, see Equation (16). [b] Values obtained from the antisymmetric part of the PECD images, see Equation (23). A stands for Abel-transformed data and $\oplus$ for the whole measured distribution within an energy range from approx. 0–1.1 eV.

Table 4. Averaged Legendre coefficients from fenchone and norcamphor.

Legendre polynomial[a]	(S)-(+)-fenchone LCP[b] averaged	(R)-(−)-fenchone LCP[b] averaged	Quantification[c]		(S)-(+)-norcamphor LCP[b] averaged	(RAC.)-(+/−)-norcamphor LCP[b] averaged	Quantification[c]	
c_0	1.000	1.000	$LPECD^{A^{-1}}_{\odot(+)}$	−13.8%	1.000	1.000	$LPECD^{A^{-1}}_{\odot(+)}$	6.7%
c_1	−0.067	0.055	$LPECD^{A^{-1}}_{\oplus(+)}$ [d]	−10.2%	0.034	−0.002	$LPECD^{A^{-1}}_{\oplus(+)}$ [d]	6.8%
c_2	−0.580	−0.558	$LPECD^{A^{-1}}_{\odot(-)}$	10.9%	−0.554	−0.516	$LPECD^{A^{-1}}_{\odot(+/-)}$	−0.5%
c_3	0.008	−0.003	$LPECD^{A^{-1}}_{\oplus(-)}$ [d]	9.1%	−0.002	0.003	$LPECD^{A^{-1}}_{\oplus(+/-)}$ [d]	0.0%
c_4	−0.061	−0.086	Quantification[e]		−0.019	−0.043	Quantification[e]	
c_5	0.004	−0.006	$QPECD^{A^{-1}}_{\odot(+)}$	13.1%	−0.006	−0.001	$QPECD^{A^{-1}}_{\odot(+)}$	6.6%
c_6	−0.008	0.001	$QPECD^{A^{-1}}_{\oplus(+)}$ [d]	9.5%	−0.008	0.011	$QPECD^{A^{-1}}_{\oplus(+)}$ [d]	6.5%
c_7	−0.001	0.000	$QPECD^{A^{-1}}_{\odot(-)}$	10.6%	0.001	−0.001	$QPECD^{A^{-1}}_{\odot(+/-)}$	0.5%
c_8	0.014	0.007	$QPECD^{A^{-1}}_{\oplus(-)}$ [d]	8.5%	−0.020	−0.005	$QPECD^{A^{-1}}_{\oplus(+/-)}$ [d]	0.2%

[a] See Equation (1). [b] Coefficients derived as described in Table 2. [c] LPECD according to Equation (17), using the averaged coefficients ($\odot$ stands for the FWHM and A^{-1} for Abel-inverted data) for ionization with LCP light. [d] Quantification for all c_{kl}-sets in a range from approx. 0–1.1 eV (equivalent to the measured PAD image), indicated by $\oplus$ [e] QPECD derived by Equation (22), using the averaged coefficients for ionization with LCP light. After deriving the quantitative measures the calculated coefficients are rounded to three decimal places.

Figure 13. For the racemic species no structured antisymmetric components emerge. In contrast to this, the *S*-norcamphor shows a strong and structured PECD effect (as discussed above). The quantitative results from the Abel-projected data are listed in Table 3 and the quantitative values from the Abel-inverted PECD images are given in Table 4. All derived quanti-

(s)-(+)-Norcamphor   **(rac)-(+/−)-Norcamphor**
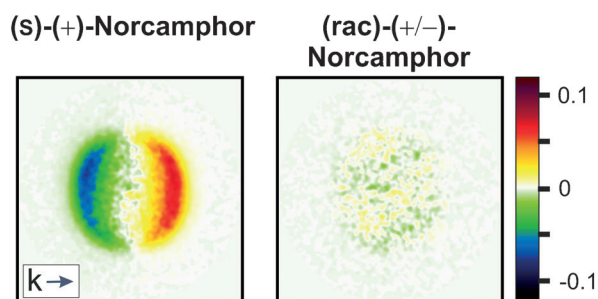
Figure 13. Antisymmetric part of the PECD images from (*S*)-(+)-norcamphor (left) and (RAC)-(+/−)-norcamphor (right). Note that in contrast to *s*-norcamphor the racemic mixture shows no distinctive antisymmetric components.

tative PECD values for (*S*)-(+)-norcamphor are in the range of 6.7 % to 7.5 % whereas for (RAC)-(+/−)-norcamphor all values are well below 1 %. These non-vanishing values for the PECD of (RAC)-(+/−)-norcamphor could originate from a small remaining enantiomeric excess or other experimental imperfections.

Recently, the identification of enantiomers in mixtures of chiral molecules prepared in a seeded molecular beam was demonstrated using broadband microwave spectroscopy[94] and three-wave mixing.[95] In mixtures of carvone differences of 20 % *ee* of the *R*-species and 33 % *ee* of the *S*-species could be distinguished when compared to the racemic mixture.[94] In mixtures of 1,2-propanediol, the racemic mixture could be distinguished from a mixture of 2 % *ee* of the *S*-species.[95]

We believe that our ionization method on effusive samples delivers at least a similar sensitivity, where substances having the same mass like camphor and fenchone could be distinguished via different excess energies of the released photoelectrons and substances having the same excess energy but different masses could be distinguished with the help of coincidence techniques. A detailed comparison of the approaches has to wait until both approaches are further developed.

4. Conclusions

In this article we have demonstrated a circular dichroism effect in the ±10 % regime derived from images of photoelectron angular distributions resulting from resonance enhanced multiphoton ionization of randomly oriented chiral molecules in the gas phase. Camphor, fenchone and norcamphor were chosen as prototypes. We observed pronounced differences in the PECD despite the similarity of their chemical structure. This may hint to the importance of the scattering state for this relative low kinetic energy electrons released in the multiphoton

process. We also noted the sensitivity of the PECD effect to enantiomeric excess.

We gave a comprehensive description and characterization of our experimental set-up as well as a detailed description of our data analysis. For circular polarization we employ an Abel inversion to expand the measured PAD images into a series of Legendre polynomials. For elliptical polarization we use tomographic data recording after we demonstrated equivalence of the two approaches for circularly polarized light. We noted that the wealth of information obtained in the projected images under many different angles used for tomographic reconstruction might be a route to a complete determination of the photoionization dynamics of chiral molecules.

We derived different measures to quantify the PECD effect by a single number for different circumstances. A linear PECD (LPECD) was derived as an extension to one-photon PECD quantifications as proposed in the literature. This LPECD contains an alternating sum of odd Legendre polynomials. Furthermore, a quadratic PECD (QPECD) was suggested which is inherently immune against cancellation effects that might occur in the LPECD owing to the alternating sum. Finally, the power PECD (PPECD) was introduced as a practical measure for cases where an Abel transform cannot be performed. For elliptical polarization we found a nonlinear relation between the Stokes S_3 parameter and the PPECD.

Intensity studies with respect to multiphoton power laws and comparison of mass spectra to PECD data revealed dissociative ionization as the origin of the observed PECD effect. On the excess energy of the PADs from the chiral molecules no ponderomotive shift was observed with increasing intensity, whereas PADs from xenon showed the expected shifts in the studied intensity range. Therefore, we conclude that ionization out of the intermediate resonance is dominating the signal and direct ionization out of the ground state seems not to contribute to the PECD effect.

We compared our results to other recently published results and found good agreement with respect to the absolute values of the contributing odd Legendre polynomials for the camphor prototype. The retrieved Legendre coefficients for the investigated bicyclic ketones may therefore serve as a benchmark for theoretical developments.

We believe that our table-top laser-based approach opens the door to many analytical applications and comparison to ab initio quantum calculations will open an additional route to determine the absolute configuration. Also an exploration of the nuclear and electron dynamics of the intermediate resonance based on coherent control techniques might help in that respect and may stimulate the development of laser-driven purification schemes.

Acknowledgements

[1] D. Patterson, M. Schnell, *Phys. Chem. Chem. Phys.* **2014**, *16*, 11114–11123.

[2] D. Patterson, M. Schnell, J. M. Doyle, *Nature* **2013**, *497*, 475–478.

[3] R. Li, R. Sullivan, W. Al-Basheer, R. M. Pagni, R. N. Compton, *J. Chem. Phys.* **2006**, *125*, 144304.

[4] U. Boesl von Grafenstein, A. Bornschlegl, *ChemPhysChem* **2006**, *7*, 2085–2087.

[5] H. G. Breunig, G. Urbasch, P. Horsch, J. Cordes, U. Koert, K.-M. Weitzel, *ChemPhysChem* **2009**, *10*, 1199–1202.

[6] U. Boesl, A. Bornschlegl, C. Logé, K. Titze, *Anal. Bioanal. Chem.* **2013**, *405*, 6913–6924.

[7] M. Pitzer, M. Kunitski, A. S. Johnson, T. Jahnke, H. Sann, F. Sturm, L. P. H. Schmidt, H. Schmidt-Böcking, R. Dörner, J. Stohner, J. Kiedrowski, M. Reggelin, S. Marquardt, A. Schießer, R. Berger, M. S. Schöffler, *Science* **2013**, *341*, 1096–1100.

[8] P. Herwig, K. Zawatzky, M. Grieser, O. Heber, B. Jordon-Thaden, C. Krantz, O. Novotny, R. Repnow, V. Schurig, D. Schwalm, Z. Vager, A. Wolf, O. Trapp, H. Kreckel, *Science* **2013**, *342*, 1084–1086.

[9] B. Ritchie, *Phys. Rev. A* **1976**, *13*, 1411–1415.

[10] L. Nahon, G. A. Garcia, C. J. Harding, E. Mikajlo, I. Powis, *J. Chem. Phys.* **2006**, *125*, 114309.

[11] N. Böwering, T. Lischke, B. Schmidtke, N. Müller, T. Khalil, U. Heinzmann, *Phys. Rev. Lett.* **2001**, *86*, 1187–1190.

[12] G. A. Garcia, L. Nahon, M. Lebech, J. C. Houver, D. Dowek, I. Powis, *J. Chem. Phys.* **2003**, *119*, 8781–8784.

[13] U. Hergenhahn, E. E. Rennie, O. Kugeler, S. Marburger, T. Lischke, I. Powis, G. Garcia, *J. Chem. Phys.* **2004**, *120*, 4553–4556.

[14] S. Turchini, N. Zema, G. Contini, G. Alberti, M. Alagia, S. Stranges, G. Fronzoni, M. Stener, P. Decleva, T. Prosperi, *Phys. Rev. A* **2004**, *70*, 014502.

[15] S. Stranges, S. Turchini, M. Alagia, G. Alberti, G. Contini, P. Decleva, G. Fronzoni, M. Stener, N. Zema, T. Prosperi, *J. Chem. Phys.* **2005**, *122*, 244303.

[16] I. Powis, C. J. Harding, G. A. Garcia, L. Nahon, *ChemPhysChem* **2008**, *9*, 475–483.

[17] *Chiral Recognition in the Gas Phase*, (Ed.: A. Zehnacker), CRC Press, Boca Raton, FL, **2010**.

[18] I. Powis, *Adv. Chem. Phys.* **2008**, *138*, 267–329.

[19] L. Nahon, G. A. Garcia, H. Soldi-Lose, S. Daly, I. Powis, *Phys. Rev. A* **2010**, *82*, 032514.

[20] S. Daly, I. Powis, G. A. Garcia, *J. Chem. Phys.* **2011**, *134*, 064306.

[21] G. A. Garcia, L. Nahon, S. Daly, I. Powis, *Nat. Commun.* **2013**, *4*, 2132.

[22] C. Lux, M. Wollenhaupt, T. Bolze, Q. Liang, J. Köhler, C. Sarpe, T. Baumert, *Angew. Chem. Int. Ed.* **2012**, *51*, 5001–5005; *Angew. Chem.* **2012**, *124*, 5086–5090.

[23] O. Kfir, P. Grychtol, E. Turgut, R. Knut, D. Zusin, D. Popmintchev, T. Popmintchev, H. Nembach, J. M. Shaw, A. Fleischer, H. Kapteyn, M. Murnane, O. Cohen, arXiv:1401.4101, **2014**.

[24] T. Ruchon, *private communication*, **2014**.

[25] M. Wollenhaupt, T. Baumert, *Faraday Discuss.* **2011**, *153*, 9–26.

[26] A. Assion, M. Geisler, J. Helbing, V. Seyfried, T. Baumert, *Phys. Rev. A* **1996**, *54*, 4605–4608.

[27] A. Stolow, A. E. Bragg, D. M. Neumark, *Chem. Rev.* **2004**, *104*, 1719–1757.

[28] J. Manz, J. F. Pérez-Torres, Y. Yang, *Phys. Rev. Lett.* **2013**, *111*, 153004.

[29] M. Wollenhaupt, A. Assion, O. Graefe, D. Liese, C. Sarpe-Tudoran, M. Winter, T. Baumert, *Chem. Phys. Lett.* **2003**, *376*, 457–464.

[30] T. Bayer, H. Braun, C. Sarpe, R. Siemering, P. von den Hoff, R. de Vivie-Riedle, T. Baumert, M. Wollenhaupt, *Phys. Rev. Lett.* **2013**, *110*, 123003.

[31] M. Wollenhaupt, M. Krug, J. Köhler, T. Bayer, C. Sarpe-Tudoran, T. Baumert, *Appl. Phys. B* **2009**, *95*, 245–259.

[32] T. Brixner, G. Krampert, T. Pfeifer, R. Selle, G. Gerber, M. Wollenhaupt, O. Graefe, C. Horn, D. Liese, T. Baumert, *Phys. Rev. Lett.* **2004**, *92*, 208301.

[33] M. Wollenhaupt, C. Lux, M. Krug, T. Baumert, *ChemPhysChem* **2013**, *14*, 1341–1349.

[34] M. Wollenhaupt, M. Krug, J. Köhler, T. Bayer, C. Sarpe-Tudoran, T. Baumert, *Appl. Phys. B* **2009**, *95*, 647–651.

[35] P. Hockett, M. Wollenhaupt, C. Lux, T. Baumert, *Phys. Rev. Lett.* **2014**, *112*, 223001.

[36] N. Bhargava Ram, C. S. Lehmann, M. H. M. Janssen, *EPJ Web Conf.* **2013**, *41*, 02029.

[37] C. S. Lehmann, N. B. Ram, I. Powis, M. H. M. Janssen, *J. Chem. Phys.* **2013**, *139*, 234307.

[38] M. H. M. Janssen, I. Powis, *Phys. Chem. Chem. Phys.* **2014**, *16*, 856–871.

[39] K. L. Reid, *Ann. Rev. Phys. Chem.* **2003**, *54*, 397–424.

[40] J. Cooper, R. N. Zare, *J. Chem. Phys.* **1968**, *48*, 942–943.

[41] U. Fano, D. Dill, *Phys. Rev. A* **1972**, *6*, 185–192.

[42] Y. Gontier, N. K. Rahman, M. Trahin, *J. Phys. B* **1975**, *8*, 179–182.

[43] S. N. Dixit, P. Lambropoulos, *Phys. Rev. A* **1983**, *27*, 861–874.

[44] C. N. Yang, *Phys. Rev.* **1948**, *74*, 764–772.

[45] S. N. Dixit, V. McKoy, *J. Chem. Phys.* **1985**, *82*, 3546–3553.

[46] S. T. Manson, A. F. Starace, *Rev. Mod. Phys.* **1982**, *54*, 389–405.

[47] B. Ritchie, *J. Chem. Phys.* **1974**, *60*, 898–907.

[48] J. W. Davenport, *Phys. Rev. Lett.* **1976**, *36*, 945–949.

[49] I. Powis, *J. Phys. Chem. A* **2000**, *104*, 878–882.

[50] I. Powis, *J. Chem. Phys.* **2000**, *112*, 301–310.

[51] M. Tia, B. C. de Miranda, S. Daly, F. Gaie-Levrel, G. A. Garcia, I. Powis, L. Nahon, *J. Phys. Chem. Lett.* **2013**, *4*, 2698–2704.

[52] L. D. Barron, *Molecular Light Scattering and Optical Activity, 2nd ed.*, University Press, Cambridge, **2004**.

[53] G. A. Garcia, L. Nahon, I. Powis, *Rev. Sci. Instrum.* **2004**, *75*, 4989–4996.

[54] S. Turchini, D. Catone, N. Zema, G. Contini, T. Prosperi, P. Decleva, M. Stener, F. Rondino, S. Piccirillo, K. C. Prince, M. Speranza, *ChemPhysChem* **2013**, *14*, 1723–1732.

[55] M. Wollenhaupt, A. Assion, T. Baumert in *Springer Handbook of Lasers and Optics, 2nd ed.*, (Ed.: F. Träger), Springer, Berlin, **2012**.

[56] A. T. J. B. Eppink, D. H. Parker, *Rev. Sci. Instrum.* **1997**, *68*, 3477–3484.

[57] W. C. Wiley, I. H. McLaren, *Rev. Sci. Instrum.* **1955**, *26*, 1150–1157.

[58] V. Schyja, T. Lang, H. Helm, *Phys. Rev. A* **1998**, *57*, 3692–3697.

[59] D. Feldmann, D. Petring, G. Otto, K. H. Welge, *Z. Phys. D* **1987**, *6*, 35–42.

[60] M. Born, E. Wolf, *Principles of Optics: Electromagnetic Theory of Propagation, Interference and Diffraction of Light, 7th ed.*, Cambridge University Press, Cambridge, **1999**, pp. 1–952.

[61] W. A. Shurcliff, *Polarized Light: Production and Use*, Harvard University Press, Cambridge, **1962**, pp. 1–207.

[62] B. Schaefer, E. Collet, R. Smyth, D. Barret, F. Beth, *Am. J. Phys.* **2007**, *75*, 163–168.

[63] J.-P. Grandin, X. Husson, *J. Phys. B* **1981**, *14*, 433–440.

[64] S. M. Koeckhoven, W. J. Buma, C. A. de Lange, *Phys. Rev. A* **1995**, *51*, 1097.

[65] NIST, http://webbook.nist.gov, **2014**.

[66] A. Bornschlegl, C. Logé, U. Boesl, *Chem. Phys. Lett.* **2007**, *447*, 187–191.

[67] P. Horsch, G. Urbasch, K.-M. Weitzel, D. Kröner, *Phys. Chem. Chem. Phys.* **2011**, *13*, 2378–2386.

[68] I. Dreissigacker, M. Lein, *Phys. Rev. A* **2014**, *89*, 053406.

[69] A. C. Kak, M. Slaney, *Principles of Computerized Tomographic Imaging*, IEEE, New York, **1999**, pp. 1–339.

[70] D. S. Weinberg, C. Djerassi, *J. Org. Chem.* **1966**, *31*, 115–119.

[71] L. Banares, T. Baumert, M. Bergt, B. Kiefer, G. Gerber, *J. Chem. Phys.* **1998**, *108*, 5799–5811.

[72] R. R. Freeman, P. H. Bucksbaum, H. M. Milchberg, S. Darack, D. Schumacher, M. E. Geusic, *Phys. Rev. Lett.* **1987**, *59*, 1092.

[73] R. Wiehle, B. Witzel, H. Helm, E. Cormier, *Phys. Rev. A* **2003**, *67*, 063405.

[74] G. N. Gibson, R. R. Freeman, T. J. McIlrath, *Phys. Rev. Lett.* **1992**, *69*, 1904–1907.

[75] D. Geißler, T. Weinacht, *Phys. Rev. A* **2014**, *89*, 013408.

[76] W. D. M. Lunden, P. Sándor, T. C. Weinacht, T. Rozgonyi, *Phys. Rev. A* **2014**, *89*, 053403.

[77] C. Lux, M. Wollenhaupt, C. Sarpe, T. Baumert, *publication in preparation*.

[78] A. Vredenborg, C. S. Lehmann, D. Irimia, W. G. Roeterdink, M. H. M. Janssen, *ChemPhysChem* **2011**, *12*, 1459–1473.

[79] C. S. Lehmann, N. B. Ram, M. H. M. Janssen, *Rev. Sci. Instrum.* **2012**, *83*, 093103.

[80] Lehmann, C. S., PhD Thesis, Vrije Universiteit Amsterdam, **2013**.

[81] V. Schurig, H.-P. Nowotny, *Angew. Chem. Int. Ed. Engl.* **1990**, *29*, 939–957; *Angew. Chem.* **1990**, *102*, 969–986.

[82] U. Ravid, E. Putievsky, I. Katzir, R. Ikan, *Flavour Fragrance J.* **1992**, *7*, 169–172.

[83] F. Pulm, J. Schramm, J. Hormes, S. Grimme, S. D. Peyerimhoff, *Chem. Phys.* **1997**, *224*, 143–155.

[84] J. W. Driscoll, T. Baer, T. J. Cornish, *J. Mol. Struct.* **1991**, *249*, 95–107.

[85] E. E. Rennie, I. Powis, U. Hergenhahn, O. Kugeler, G. Garcia, T. Lischke, s. Marburger, *J. Electron Spectrosc. Relat. Phenom.* **2002**, *125*, 197–203.

[86] M. Getzlaff, G. Schönhense, *J. Electron Spectrosc. Relat. Phenom.* **1998**, *95*, 225–230.

[87] D. C. Frost, N. P. C. Westwood, N. H. Werstiuk, *Can. J. Chem.* **1980**, *58*, 1659–1666.

[88] D. Chadwick, D. C. Frost, L. Weiler, *J. Am. Chem. Soc.* **1971**, *93*, 4962–4963.

[89] G. Hentrich, E. Gunkel, M. Klessinger, *J. Mol. Struct.* **1974**, *21*, 231–244.

[90] A. Assion, T. Baumert, J. Helbing, V. Seyfried, G. Gerber, *Chem. Phys. Lett.* **1996**, *259*, 488–494.

[91] C. J. Harding, E. Mikajlo, I. Powis, S. Barth, S. Joshi, V. Ulrich, U. Hergenhahn, *J. Chem. Phys.* **2005**, *123*, 234310.

[92] I. Powis, *Chirality* **2008**, *20*, 961–968.

[93] C. Lux, S. Züllighoven, A. Kastner, T. Ring, C. Sarpe, M. Wollenhaupt, A. Senftleben, T. Baumert, *publication in preparation*.

[94] V. A. Shubert, D. Schmitz, D. Patterson, J. M. Doyle, M. Schnell, *Angew. Chem. Int. Ed.* **2014**, *53*, 1152–1155; *Angew. Chem.* **2014**, *126*, 1171–1174.

[95] D. Patterson, J. M. Doyle, *Phys. Rev. Lett.* **2013**, *111*, 023008.